Competence for transcellular infection in the root cortex involves a post-replicative, cell-cycle exit decision in *Medicago truncatula*.

Morgane Batzenschlager[1,*], Beatrice Lace[1], Ning Zhang[1,2], Chao Su[1], Sabrina Egli[1], Pascal Krohn[1,3], Jule Salfeld[1], Franck Anicet Ditengou[1,4], Thomas Laux[1,2], and Thomas Ott[1,3,*].

[1] *University of Freiburg, Faculty of Biology, 79104 Freiburg, Germany*

[2] *CIBSS – Centre of Integrative Biological Signalling Studies, University of Freiburg, Freiburg, Germany*

[3] *present address: Max Planck Institute for Plant Breeding Research, Department for Plant-Microbe Interactions, 50829 Cologne, Germany*

[4] *present address: Freiburg University Medical Centre, Institute for Disease Modelling and Targeted Medicine (IMITATE 79106 , Freiburg, Germany*

*Corresponding authors:

morgane.batzenschlager@biologie.uni-freiburg.de; thomas.ott@biologie.uni-freiburg.de

ABSTRACT

During root nodule symbiosis (RNS), cell-division activity is re-initiated and sustained in the root cortex to create a hospitable cellular niche. Such temporary and spatially confined site is required to render host cells compatible with the intracellular progression of rhizobia. Although it has been suggested that early infection events might involve a pre-mitotic cell-cycle arrest, this process has not been dissected with cellular resolution. Here, we show that a dual-colour Medicago histone reporter robustly identifies cells with different mitotic or endoreduplication activities in the root cortex. By imaging deep root tissues, we found that a confined trajectory of cortical cells that are

transcellularly passed by infection threads are in a stage of the cell-cycle that is distinct from directly adjacent cells. Distinctive features of infected cells include nuclear widening and large-scale chromatin rearrangements consistent with a cell-cycle exit prior to differentiation. Using a combination of fluorescent reporters demarcating cell-cycle phase progression, we confirmed that a reduced proliferation potential and modulating the G2/M transition, a process possibly controlled by the NF-YA1 transcription factor, mark the success of rhizobial delivery to nodule cells.

INTRODUCTION

Cell-cycle regulation is a key pathway to maintain beneficial and sustainable symbiotic associations that are of primary importance in both marine and terrestrial ecosystems. One common theme to stabilize facultative associations is to achieve a mutual control of cell proliferation and differentiation dynamics in both the host and the symbionts (Kondorosi & Kondorosi, 2004; Russo & Genre, 2021; Rivera & Davies, 2021). Prime examples are flowering plants from a single phylogenetic clade, comprising four orders (Fabales, Fagales, Cucurbitales, Rosales) with legumes being the most prominent ones, that evolved the unique ability to accommodate soil-borne rhizobia intracellularly (Parniske, 2018). Within this symbiosis, rhizobia fix atmospheric nitrogen and deliver ammonium to the host in exchange for plant photosynthates. The conversion of atmospheric dinitrogen into a usable form is highly energy-demanding and requires a low-oxygen environment, which is provided within nodules, specialized lateral organs formed on the roots that are densely populated by rhizobia. A widely adopted mechanism to access the developing nodule cells is the formation of cortical infection threads, transcellular conduits formed upon the invagination of the host plasma membrane and hijacking the cellular machinery of infected root cortical cells (Timmers et al., 1999; Su et al., 2023). Although our molecular and cellular understanding of the infection mechanisms is expanding (Tsyganova et al., 2021; Monroy-Morales et al., 2022; Gao et al., 2022), our knowledge on how these processes are interconnected with the control of cell-cycle progression in cells hosting intracellular infection threads has remained fragmentary.

52 Plants engaging into arbuscular mycorrhizal (AM) or root nodule symbioses (RNS) have
53 recruited a common range of cell-cycle processes (Foucher & Kondorosi, 2000; Russo & Genre,
54 2021). In *M. truncatula* (hereafter, Medicago) the perception of and colonization by the AM fungus
55 result in occasional cell divisions in the inner cortical layers (Russo et al., 2019) and in diffuse
56 endoreduplication events as intraradical hyphae spread throughout the root cortex (Carotenuto et al.,
57 2019a; Carotenuto et al., 2019b). During RNS, the perception of rhizobia results in the onset of a
58 signalling cascade that triggers an outward gradient of cell-cycle reactivation and cell divisions.
59 Although this is initiated in the pericycle, cell-cycle reactivation occurs throughout the inner cortical
60 (C) layers C5, C4 and the middle C3 layer in Medicago (Timmers et al., 1999; Xiao et al., 2014). The
61 successful establishment of RNS further involves the tight coordination of the infection and
62 organogenesis programmes (Guan et al., 2013; Madsen et al., 2010). It requires the progression of
63 cortical infection threads through the C3 layer prior to subsequent periclinal divisions that produce a
64 persistent nodule meristem (Xiao et al., 2014). The resulting indeterminate nodules will later form
65 well-defined developmental zones, with actively dividing meristematic cells giving rise to post-
66 meristematic, differentiating central tissues of increasing ploidy (Vinardell et al., 2003; Nagymihály
67 et al., 2017). While those cells can be intracellularly colonized, the infection competence of nodule-
68 like structures as being induced by exogenous application of cytokinin (Gauthier-Coles et al., 2019),
69 constitutive activation of common symbiotic components (Gleason et al., 2006; Ried et al., 2014;
70 Singh et al., 2014) or the expression of meristematic factors (Dong et al., 2021) may be massively
71 reduced in many of these spontaneous nodules (Hayashi et al., 2010; Liu et al., 2022). The lack of
72 infectibility cannot be overcome even when applying bacterial strains which enter plant cells from
73 the intercellular space (Liang et al., 2019). This clearly demonstrates the ultimate requirement of cells
74 being in a so far uncharacterized state of infection competence.

75 Transcriptome profiling of Medicago root hairs, treated with rhizobial Nod factors or
76 undergoing rhizobial colonization, uncovered changes in several cell-cycle related genes (Breakspear
77 et al., 2014; Liu et al., 2019a). This perception of Nod factors results in the increased transcription of

78 D-type cyclins, genes known to respond to extrinsic signals and to promote cell-cycle progression
79 from the first GAP (G1) phase to the DNA-synthesis (S) phase (Soni et al., 1995; Dewitte et al.,
80 2003). Subsequently, the initiation of infection threads coincides with the highest expression of genes
81 required for DNA replication, modification and repair, strongly suggesting that the epidermal
82 infection programme involves cell cycle re-entry and progression to a post-replicative phase
83 (Breakspear et al., 2014). A repression of the endocycle was further proposed to occur since infected
84 root hairs accumulate transcripts of the *OSD1/UVI4* gene (Breakspear et al., 2014), whose activity
85 prevents an unscheduled increase in ploidy by inhibiting the anaphase-promoting complex/cyclosome
86 (Iwata et al., 2011). However, much less is known about the transcriptional signature of infected cells
87 along the cortical trajectory of transcellularly progressing infection threads. Such ability to guide
88 rhizobia *via* cortical infection threads is, however, thought to be an important innovation since it has
89 been evolutionary maintained in the vast majority of nodulating species as it, most likely, maximizes
90 the host control over bacterial delivery (Parniske, 2018; Cathebras et al., 2022 – pre-print).
91 A central regulator for controlling infection and organogenesis is the transcription factor
92 *Nodule Inception* (*NIN*). Co-opted from nitrate response circuits, NIN acts as a master coordinator of
93 infection, nodule organogenesis and nodule number (Schauser et al., 1999; Marsh et al., 2007;
94 Fournier et al., 2015; Soyano et al., 2014; Cathebras et al., 2022 – pre-print). It promotes the
95 expression of several growth targets (Liu et al., 2019a) including *NF-YA1* (Soyano et al., 2013; Feng
96 et al., 2021), a subunit of the conserved heterotrimeric Nuclear Factor-Y (NF-Y) transcription factor.
97 A-, B- and C-type subunits of the NF-Y complex act as specialized modules, interacting with other
98 transcription factors and recruiting chromatin remodelling enzymes to adjust cell specification to
99 environmental or developmental needs (Baudin et al., 2015; Zanetti et al., 2016; Myers & Holt, 2018).
100 In vertebrates, the CCAAT-binding NF-Y transcription factor targets genes involved in all major
101 activities executed in G2 and mitosis (M; Bolognese et al., 1999; Linhart et al., 2005) and is an
102 important regulator of the G2/M transition (Manni et al., 2001). In legumes, the rhizobium-induced
103 NF-YA1 subunit functions in cortical infection thread progression, in the establishment and

104 maintenance of the nodule meristem and in the early differentiation of nodule cells (Combier et al.,
105 2006; Laporte et al., 2014; Xiao et al., 2014; Shrestha et al., 2021; Schiessl et al., 2023 – pre-print).
106 Yet, whether the Medicago NF-YA1 protein regulates the G2/M transition is not known.

107 The hypothesis that intracellular infection at least partially relies on cell-cycle control is
108 further supported by structural re-arrangements in cortical cells anticipating transcellular IT
109 progression. These include the formation of pre-infection threads (PITs), which are transvacuolar,
110 cytoplasmic bridges comparable to those occurring in pre-mitotic cells (van Brussel et al., 1992;
111 Timmers et al., 1999). *In situ* detection of marker transcripts revealed that outer cortical cells recruit
112 histone H4 used during DNA replication but do not express a B-type, mitotic cyclin gene – implying
113 that activated target cells stop in the G2 phase of the cell cycle (Yang et al., 1994). G2-phase cell-
114 cycle arrests have been repeatedly described in eukaryotic cells as appropriate gates for executing
115 cell fate and patterning decisions (Meserve & Duronio, 2017; Meyer et al., 2017), for wound healing
116 (Cosolo et al., 2019) or for host infection during pathogenic and biotrophic interactions (Wildermuth
117 et al., 2017; Bardetti et al., 2019). In plants, transiently or sustainably reducing the potential to enter
118 mitosis is an appropriate response when cells must, for instance, cope with genotoxic stresses (Chen
119 et al., 2017; Takahashi et al., 2019) or switch to another cell-cycle program, such as the meiotic
120 (Hernandez-Lagana et al., 2021) or the endoreduplication cycle (De Veylder et al., 2011; Wildermuth
121 et al., 2017). Modulating the G2/M transition combines well-described transcriptional and post-
122 translational mechanisms, leading to the repression of genes necessary to execute cell division
123 (Berckmans & De Veylder, 2009; Kobayashi et al., 2015), controlling the activity of cyclin-dependent
124 kinases (CDK; Shimotohno et al., 2021) and the stability of transcriptional repressors and mitotic
125 inducers (Fülöp et al., 2005; Chen et al., 2017). Although previous reports have suggested such cell-
126 cycle patterns to occur in roots during rhizobial infections (Yang et al., 1994; Breakspear et al., 2014),
127 this has never been spatially resolved at cellular level.

128 Here, we employed a combination of cell-cycle reporters to resolve functional steps of cell-
129 cycle progression on the cortical infection thread trajectory with cellular and subcellular resolution.

130 We demonstrate that the first generation of Medicago cells successfully internalizing rhizobia shows
131 unique features, including a marked decrease in their histone H3.1 content and a reduced competence
132 for both cell division and chromosome segregation. We also show that tetraploid (4n) cells reaching
133 an 8C DNA content are optimal for infection by rhizobia. Our results reveal that, upon transcellular
134 infection thread passage, cortical cells undergo a last GAP phase after DNA replication and exit to
135 differentiation. Furthermore, we present first evidence that the symbiotically-induced NF-YA1
136 subunit, by controlling mitotic entry in a heterologous system, holds potential to contribute to this
137 process.
138

139 **RESULTS**

140 ***A reduced proliferative potential typifies cells supporting cortical infection thread progression***

141 In *A. thaliana* (hereafter, Arabidopsis), the incorporation and eviction dynamics of histone H3
142 variants have been used to identify cells with different cell division and reprogramming potentials,
143 during organ patterning (Otero et al., 2016) or when acquiring reproductive competence (Lagana &
144 Autran, 2020). To test whether gaining a stage of intracellular infection competence involves a similar
145 modification of the cell-division potential and associated chromatin reorganization, we searched for
146 Medicago genes coding for the replicative histone variant H3.1 and the replacement variant H3.3
147 (Figure 1–figure supplement 1A; Probst et al., 2020). The encoded Medicago H3.1 protein is identical
148 to the one present in *L. japonicus* and *H. vulgare* and, as in other flowering plants, differs from H3.3
149 by only four residues (Figure 1–figure supplement 1B; Shi et al., 2011; Lu et al., 2018). To check
150 that these Medicago *H3* genes encode for *bona fide* H3.1 and H3.3 counterparts, native promoter-
151 genomic fusions with fluorescent tags were expressed in *A. rhizogenes*–induced transgenic roots,
152 formed on plants that were inoculated with the compatible symbiont *S. meliloti*. We adopted a
153 fixation, clearing and cell-wall counter-staining procedure (Ursache et al., 2018) that enabled us to
154 perform detailed imaging deep inside the multi-layered root cortical tissues. Medicago H3 fusion
155 proteins fully recapitulated the patterns observed in Arabidopsis roots (*i.e.,* patchy pattern of H3.1

156 and constitutive presence of H3.3; Figure 1–figure supplement 1C–E) and showed the expected
157 localization in euchromatin (diffuse labelling) and heterochromatic regions (subnuclear foci; Figure
158 1–figure supplement 1C–E; Ingouff et al., 2010; Shi et al., 2011; Otero et al., 2016). A low H3.1
159 content, typical for cells with a reduced proliferative potential, also enabled us to identify putative
160 quiescent centre (QC) cells within the open root apical meristem of Medicago (Figure 1–figure
161 supplement 1E; Rost, 2011; Otero et al., 2016; Xiao et al., 2019; Ghahremani & MacLean, 2020).
162 Preferentially incorporated during DNA replication, the canonical histone H3.1 variant controls the
163 maintenance of genome integrity (Davarinejad et al., 2022) and epigenetic inheritance (Jiang &
164 Berger, 2017) and is consequently maintained at high levels in cells engaged in recurrent cell division
165 or endoreduplication cycles (Figure 1A). Once cells exit the cell cycle, H3.1 is evicted and likely
166 replaced by H3.3 to mediate cellular differentiation in various Arabidopsis cell types (Otero et al.,
167 2016). In Medicago, increased levels of *H3.1* transcripts were coherently detected at an early stage
168 of nodule primordia development (Figure 1– figure supplement 1F; Schiessl et al., 2019) and mRNAs
169 accumulate only in meristematic (ZI) and infection zones of mature nodules (ZIId and ZIIp; Roux et
170 al., 2014), while *H3.3* transcription stayed high in the differentiation zone (ZIII; Figure 1– figure
171 supplement 1G). We verified a corresponding differential accumulation of H3.1 and H3.3 tagged
172 proteins at cellular resolution in nodule sections (Figure 1B). The double histone reporter proved also
173 useful to distinguish actively endoreduplicating cells prior to fungal colonization (Carotenuto et al.,
174 2019; Carotenuto et al., 2019a) from fully differentiated, arbuscule-containing cells (Figure 1C).
175 Since the selected Medicago histone variants recapitulated the expected transcriptional and
176 localization patterns in well-defined developmental zones, we considered them as functional reporters
177 of H3.1 and H3.3. In addition, the H3.1/H3.3 balance enables to track cortical cells re-entering the
178 cell cycle and adapting their responses to both bacterial and fungal symbionts.

179 We then focused on the H3.1 nuclear content at early interaction stages between rhizobia and
180 the host plant (8 days post inoculation [dpi]; Figure 2A–B). In accordance with RNA sequencing data
181 (Figure 1– figure supplement 1F; Schiessl et al., 2019), we observed the replicative H3.1 variant

182 accumulating in regularly dividing cortical cells forming the nodule primordium (Figure 2A, left
183 panel). The H3.1-eGFP fusion protein was also visible in cells penetrated but not fully passed by an
184 infection thread (Figure 2A, close up). This is consistent with earlier observations that cells preparing
185 for intracellular infection pass through S-phase (Yang et al., 1994). By contrast, host cells sustaining
186 cortical infection thread progression in the middle and inner cortex (C3 and C4) up to the first
187 recipient cells in the nodule primordium (C4/5-derived; Figure 2B) exhibited enlarged nuclei (Figure
188 2C) with a significantly decreased histone H3.1 content compared to their direct neighbouring cells
189 (Figure 2D). Such pattern was also observed using another *H3.1* gene expressed in root tissues (*H3.1*
190 *(2)*; Figure 2–figure supplement 1A–E). Nuclear enlargement associated with a massive eviction of
191 H3.1 typically identifies cells having completed a DNA replication round, but pausing in the
192 following GAP phase for cell-cycle switches or exit decisions (Figure 2E; Otero et al., 2016; Lagana
193 & Autran, 2020; Probst et al., 2020). Together, our data strongly suggest that cortical cells along the
194 infection thread trajectory, different to their direct neighbours, exhibit a reduced proliferation
195 potential and presumably exit the cell cycle (Figure 2 B–E). The observed nuclear enlargement and
196 large-scale chromatin rearrangements are consistent with an increased transcriptional activity
197 (Knaack et al., 2022) concomitant with sustained infection thread progression (Breakspear et al.,
198 2014; Liu et al., 2019a). This proves the long-standing hypothesis that cortical cells competent for
199 transcellular infection suspend their course in G2 (Yang et al., 1994; Timmers et al., 1999) in
200 Medicago.

201

202 ***Exiting the cell cycle on the cortical infection thread trajectory aligns infection and organogenesis***
203 Next, we tested whether a cell-cycle exit decision and associated remodelling of the histone H3
204 composition requires the tight coupling of infection and nodule organogenesis as observed under
205 wild-type (WT) conditions. Thus, we compared the H3.1/H3.3 patterns in WT roots to those of two
206 mutants in which nodule organogenesis is either abolished (*daphne-like*; Liu et al., 2019b) or where
207 nodules form but cortical infection threads are impaired in their progression (*nf-ya1-1*; Laporte et al.,

208 2014). In the WT situation, the majority of cortical cells (90%) enabling transcellular passage until
209 reaching the nodule primordium showed a reduced proliferation potential (low H3.1 content, n = 41;
210 Figure 3A and Figure 3–figure supplement 1A). A higher H3.1 content was occasionally observed in
211 the last infected cell in the absence of nodule primordium organogenesis (NOD $^{(-)}$; Figure 3–figure
212 supplement 1B). Absence of inner cortical cell division is also a characteristic feature of the *daphne-*
213 *like* Medicago mutant (Figure 3–figure supplement 1C), which lacks a remote cis-regulatory region
214 in the *NIN* promoter perceiving cytokinin signals (Liu et al., 2019b). This non-nodulating mutant still
215 produces WT-like root hair infections occasionally reaching outer cortical layers. In this context, the
216 percentage of infected cortical cells visibly accumulating H3.1 in the euchromatin increased from
217 10% in the WT to almost 41% in the *daphne-like* mutant (n = 44; Figure 3A and Figure 3–figure
218 supplement 1D). This indicates that outer cortical cells hosting an infection thread lack an extensive
219 chromatin reorganization in the absence of sustained nodule organogenesis.
220 As a second mutant, we chose a *nf-ya1* null allele, producing smaller nodules that are additionally
221 delayed and impaired in their development (Laporte et al., 2014; Xiao et al., 2014). Nodule primordia
222 of the *nf-ya1-1* mutant showed reduced cell layers, with a lower frequency of cell divisions in the
223 inner cortex (C4/5) and only few anticlinal divisions in the middle layer (C3; Figure 3–figure
224 supplement 1E-G; Xiao et al., 2014; Schiessl et al., 2023 – pre-print). Cortical infection threads
225 appeared abnormally bulbous (Figure 3A and Figure 3–figure supplement 1E-F) and showed signs
226 of early abortion (Figure 3–figure supplement 1G; Laporte et al., 2014; Schiessl et al., 2023 – pre-
227 print). We observed that, even though the majority (76%) of crossed cortical cells were presumably
228 arrested in a GAP phase (low H3.1 content, n = 54; Figure 3–figure supplement 1F), such pausing
229 was not observed in about 24% of the inspected events. Here, infection threads were either blocked
230 or delayed in the outer cortex and the replicative H3.1 variant was retained (Figure 3A and Figure 3–
231 figure supplement 1G). Although the last infected cortical cells showed a significant nuclear
232 enlargement in all three genetic backgrounds investigated (Figure 3B), failure to coordinate
233 organogenesis and infection programs in the mutants resulted in an increased occurrence of infected

234 cells accumulating more H3.1 than their direct neighbours (Figure 3C). Together, these data reveal
235 that an appropriate reduction in cell-cycle activity and associated chromatin changes in infected cells
236 coincide with an efficient progression of cortical infection threads.
237
238 ***Cortical cells supporting transcellular infection control their commitment to cell division***
239 In Medicago and other plants producing indeterminate nodules, a local control of mitotic activity
240 could be especially important for rhizobia to timely cross the middle cortex, where sustained cellular
241 proliferation gives rise to the nodule meristem (Xiao et al., 2014). To investigate in greater detail
242 whether cells competent for transcellular infection are selectively kept away from transiting to
243 mitosis, we first used a triple fluorescent sensor enabling to track all cell-cycle phases *in planta*.
244 Originally developed for Arabidopsis, the plant cell-cycle indicator (PlaCCI) combines a component
245 of the pre-replication complex (CDT1a), the replicative histone variant (H3.1) and the N-terminal
246 domain of a B-type cyclin (N-CYCB1;1) as G1-, S- and late G2-phase reporters, respectively (Figure
247 4A; Desvoyes et al., 2020; Echevarria et al., 2021). The N-terminal domain of CYCB1;1 contains a
248 destruction box (D-box) ensuring a rapid turnover of the protein after one mitotic cell cycle (Colón-
249 Carmona et al., 1999). These cell-cycle markers are expressed at early stages of organ development
250 but disappear in terminally differentiated cells (Desvoyes et al., 2020). When expressing the PlaCCI
251 construct in transgenic Medicago roots, all three markers were successfully visualized in reactivated
252 cortical cells upon nodule primordium formation (Figure 4B–C). Cortical cells crossed by an infection
253 thread kept low but detectable amounts of the Arabidopsis H3.1 variant, indicating that they transited
254 through S-phase (Figure 4C). However, these cells stopped before accumulating substantial levels of
255 N-CYCB1;1, in contrast to their direct neighbours. We also confirmed latter observations when using
256 an Arabidopsis CYCB1;2-based fluorescent reporter (Figure 4D; Trolet et al., 2019), labelling only
257 cells that transit through G2/M (Figure 4–figure supplement 1A; Weimer et al., 2016). Together, these
258 results verified a selective decrease in mitotic competence occurring on the cortical infection thread
259 trajectory (Yang et al., 1994) as rhizobia pass the middle cortical layer (C3) in Medicago roots.

260 Importantly, we did not observe the G1-phase marker accumulating in cells undergoing infection
261 (Figure 4C), favouring the hypothesis of a cell-cycle arrest and exit decision (Figure 2E) rather than
262 a rapid switch to another endoreduplication round (Desvoyes et al., 2019 – pre-print).

263 We next tested whether transcriptional reporters of a target gene necessary to execute cell
264 division get selectively repressed on the path of a cortical infection. The late G2/M gene *KNOLLE*
265 codes for a syntaxin protein specialized in angiosperm cytokinesis (Park et al., 2018) and is oppositely
266 controlled when cells do (Haga et al., 2007) or shall not (Takahashi et al., 2019) commit to mitosis.
267 The transcription of *KNOLLE* and other late cell-cycle genes (*e.g.*, *CYCB1;2*) in Arabidopsis is
268 primarily regulated by mitosis-specific activator (MSA) cis-elements present in their promoters that
269 are targeted by activator- and repressor-type three Myb repeats (MYB3R) transcription factors (Haga
270 et al., 2007; Kobayashi et al., 2015). Mutations in all three MSA core sequences present in the
271 Medicago *KNOLLE* promoter significantly reduced the expression of a β-glucuronidase (*GUS*)
272 reporter gene in *N. benthamiana* leaf cells in the presence of a hyperactive form of a MYB3R
273 transcriptional activator (NtmybA2Δ630; Figure 4–figure supplement 1B; Araki et al., 2004),
274 suggesting that the Medicago *KNOLLE* gene can be used as a *bona fide* late G2/M readout. Using the
275 pKNOLLE::NLS-3xVenus construct we found that the activation of the *KNOLLE* promoter was
276 lower on the cortical infection thread trajectory in comparison to neighbouring, proliferating cells
277 from nodule primordia (Figure 4E). An equivalent construct, ensuring the timely elimination of
278 fluorescent reporters after one canonical cell cycle (pKNOLLE::D-box-3xVenus-NLS; Figure 4–
279 figure supplement 1C), corroborated a selective control of the G2/M transition in cells undergoing
280 transcellular infection. Combining our observations of enlarged nuclei (Figure 2C), the absence of a
281 G1 marker and the reduced H3.1 levels and expression of mitotic genes (Figure 2D and Figure 4B–
282 E), we conclude that the initial cortical cells along the infection thread trajectory conduct a single
283 cell-cycle round and stay in a post-replicative (*i.e.*, G2) phase as long as they are crossed.

284 We further took advantage of the fact that the PlaCCI sensor provides a full view on cell-cycle
285 phase progression in root tissues, in Arabidopsis (Desvoyes et al., 2020) and Medicago (this study).

286 CDT1a- and CYCB1;1-associated signals in the root tip enabled us to identify 2C (*i.e.*, G1) and 4C
287 (*i.e.*, G2) nuclei, respectively (Figure 4-figure supplement 2A) – where 2C and 4C chromatin-values
288 correspond to the DNA content of a basic diploid genome. Measuring the area of nuclei exhibiting
289 the CYCB1;1-YFP signal in cortical layers of the root apical meristem (root tip) or the nodule
290 primordium revealed that they were on average 1.57 or 1.63 times larger than the ones producing
291 CDT1a-CFP, respectively (Figure 4-figure supplement 2B). This is in agreement with an increased
292 DNA content as cells transit from the G1- to the late G2-phase. Surprisingly, proliferating nodule
293 cells contain significantly wider nuclei than their diploid counterparts in the proliferation zone of the
294 root apical meristem (Figure 4-figure supplement 2B), suggesting a higher ploidy level early on.
295 These results lead to the intriguing possibility that reactivated inner cortical cells in Medicago enter
296 the mitotic cell cycle with an increased amount of genetic material.
297
298 ***Proliferation of endopolyploid cortical cells is a distinctive feature of Medicago root nodules***
299 Our data suggest that the dividing cortical cells contributing to nodule primordium formation are
300 polyploid – *i.e.*, that they contain more than the two genome copies of a diploid (2n) cell, where "n"
301 refers to the number of separate chromosomes. To assess this further, we identified and used the
302 centromere-specific histone H3 variant (CENH3) from Medicago as a marker of individual
303 chromosomes. Such fluorescently-tagged CENH3 proteins have already been successfully applied
304 for chromosome quantification *in planta* (Lermontova et al., 2006; De Storme et al., 2016). Aligning
305 the Medicago CENH3 amino acid sequence (G8A083) with characterized CENH3 sequences from
306 *L. japonicus* (Tek et al., 2014), Arabidopsis (Talbert et al., 2002), *H. vulgare* (Sanei et al., 2011) and
307 *O. sativa* (Hirsh et al., 2009) revealed the presence of canonical CENH3 features (Figure 5–figure
308 supplement 1), including a variable N-terminal tail and the centromere targeting domain (CATD;
309 Karimi-Ashtiyani et al., 2015). When expressing a mCitrine-CENH3 fusion protein under the control
310 of its own promoter (pCENH3::mCitrine-CENH3), CENH3 labelled up to 16 nuclear foci and
311 localized exclusively at the presumed centromeres during mitosis (Figure 5A and B) in diploid root

312 tip cells. As the signal was rather weak, we scored centromeric foci in roots ectopically expressing
313 the protein (pUbi::mCitrine-CENH3; Figure 5A). Here, a reliable signal was observed in an increased
314 proportion of nuclei (82%) displaying not more than 14 to 16 mCitrine-CENH3 foci (versus only
315 55% when *CENH3* was expressed under its endogenous promoter; n = 55; Figure 5B) – reflecting the
316 base ploidy in *M. truncatula* with 2n = 16. We therefore used the pUbi::mCitrine-CENH3 reporter
317 construct for our further analyses.

318 In a first set of experiments, we used CENH3 to discriminate between polyploid cells
319 undergoing endomitosis or endocycling. In endomitosis, entire chromosome replication and partial
320 mitotic progression result in a doubling of the chromosome / centromeric foci number (Iwata et al.,
321 2011; De Storme et al., 2016). By contrast, endocycling cells undergo repeated rounds of DNA
322 synthesis without segregating the newly replicated parts (Edgar et al., 2014). Here, copied
323 chromosome arms do not condense and spatial separation of sister kinetochores does not occur, so
324 that the number of compact CENH3 signals corresponds to the initial number of chromosomes (up to
325 8C; Figure 5–figure supplement 2A; Lermontova et al., 2006). As the occurrence of endocycling cells
326 has been previously reported in tissues infected by AM fungi, we first tested the CENH3-reporter in
327 roots inoculated with *R. irregularis*. Indeed, cortical cells entered by the fungus displayed large nuclei
328 with no more than 16 labelled foci (Figure 5–figure supplement 2B), supporting their endocycling
329 nature (Carotenuto et al., 2019a; Lermontova et al., 2006). Up to 16 CENH3 foci were also observed
330 in diploid cortical cells from the root tip and pericycle cells from lateral root primordia (Figure 5–
331 figure supplement 2C). However, the majority of nodule cells exhibited between 26 and 32
332 fluorescent centromeric foci (75,5% in nodule primordia from stage IV to VI, n = 106; Figure 5–
333 figure supplement 2B–C) and a visibly increased number of chromosomes on mitotic figures (Figure
334 5–figure supplement 2B). These observations strongly support previously published data proposing
335 that proliferating cortical cells giving rise to Medicago root nodules are tetraploid (4n = 32; Wipf &
336 Cooper, 1938; Torrey & Barrios, 1969).

337 We next tested whether endopolyploid cells are already present at an earlier stage of nodule
338 development, where cell division events are confined to the pericycle, the inner cortical cells (C4,
339 C5) and occasionally occur in the third (C3) and second (C2) cortical layers (Figure 5C; Xiao et al.,
340 2014). Indeed, cells originating only from cortical cell divisions (C2 to C5) showed an increased
341 number of chromosomes (Figure 5D-E) compared to recently divided cells originating from the
342 pericycle (Figure 5E). Notably, cells performing anticlinal divisions in the middle cortex (Figure 5D,
343 left panel) that will later be crossed by the infection thread (Figure 5E, violet triangle) were also
344 polyploid. From these observations, we concluded that a key feature of cortical cells in Medicago
345 nodules is their ability to segregate a higher number of chromosome copies - corresponding to 8C in
346 a tetraploid cell entering mitosis.
347
348 ***Infected cells within the nodule primordium selectively halt their preparations for mitosis***
349 In a next set of experiments, we studied to which extent the cells positioned on the infection thread
350 trajectory (C3 to C4/5) prepare for mitosis. For this, we made use of the pre-mitotic loading
351 characteristics of CENH3 to the centromeres, which mainly occurs during the G2 phase and prior to
352 the spatial separation of sister kinetochores (Figure 6A; Lermontova et al., 2006, 2007, 2011). In
353 proliferating populations of the root tip (Figure 6–figure supplement 1A) and nodule primordia
354 (Figure 6A-B), late G2 cells contained large nuclei where the majority of sister kinetochores was split
355 and appeared as twin foci. We further noticed that centromere separation in Medicago is a gradual
356 rather than a simultaneous process, as root tip cells with comparable nuclear areas often exhibited an
357 intermediate number of fluorescent doublets (Figure 6–figure supplement 1A) of similar appearance
358 and length on a single focal plane (Figure 6–figure supplement 1B–D). To address the question to
359 which extent cortical cells that are competent for infection progress through the G2 phase and commit
360 to nuclear division, we assessed the gradual formation of sister centromeres. Although the nuclear
361 size of infected C3 cells suggested an 8C DNA content, as found in late G2-phase cells of the nodule
362 tissue (Figure 6B, C), none of these infected cells showed the typical CENH3 twin foci formed when

363 sister kinetochores split (n = 13; Figure 6B and D). Such control over mitotic commitment was tightly
364 maintained in the majority of infected, C4/5-derived cells (75,5%; n = 53; Figure 6D) which did not
365 display any visible sign of centromere separation across image stacks (Figure 6B), despite a
366 presumably duplicated genomic DNA content (Figure 6C). A smaller proportion of the recently
367 infected cells (20,7%) partially prepared for chromosome segregation and showed up to 3 fluorescent
368 doublets (Figure 6D) of comparable lengths to those measured in G2-phase progressing cells (Figure
369 6E), whereas only two cells (3,8%) with internalized bacteria got closer to nuclear and likely to cell
370 division (Figure 6B and D). Together, by combining several marker strategies based on histone H3
371 dynamics and on *bona fide* mitotic reporters, we conclude that most middle (C3) and inner (C4/5-
372 derived) cortical cells competent for intracellular infection enter a post-replicative, G2-type phase
373 without proceeding towards M-phase. Endopolyploid cortical cells hosting infection threads have
374 presumably gained the ability to execute a differentiation program rather than entering cell division
375 at the end of G2.
376
377 ***The symbiosis-specific NF-YA1 subunit holds potential to modulate the G2/M transition***
378 Our data suggest that cell-cycle progression and bacterial infection are highly coordinated, although
379 the precise molecular players able to redirect cell-cycle decisions while promoting cortical infections
380 remain to be identified. Prominent candidates are NF-YA1 proteins that were evolutionary recruited
381 to RNS where they sustain both organogenesis and intracellular infection in a range of nodulating
382 legume and non-legume species (Combier et al., 2006; Laporte et al., 2014; Xiao et al., 2014; Hossain
383 et al., 2016; Soyano et al., 2019; Bu et al., 2020; Shrestha et al., 2021). NF-YA1 plays an
384 unambiguous role as a positive regulator of cell divisions (Soyano et al., 2013) but was also recently
385 shown to function in the early differentiation and specification of nodule cells in Medicago (Schiessl
386 et al., 2023 – pre-print). This prompted us to assess whether NF-YA1 could act as a switch at mitotic
387 entry. To test this, we used WT NF-YA1 and a mutated variant lacking a functional DNA-binding
388 domain (mutDBD) as eGFP fusion proteins. As expected, both variants localized to the nucleus in *N.*

389 *benthamiana* epidermal cells (Figure 7A; Laporte et al., 2014). To foster cell cycle re-entry in such
390 differentiated cells, we ectopically expressed the Arabidopsis D-type cyclin *CYCD3;1* in mature
391 leaves as described in the recently developed 'cell division-enabled leaf system' (CDELS; Xu et al.,
392 2020). As these re-activated cells commit to mitosis and perform cytokinesis (Figure 7B), they also
393 enable the activation of promoters containing MSA cis-elements (Xu et al., 2020) as found in the
394 Medicago *KNOLLE* promoter (Figure 4–figure supplement 1B). We confirmed this by expressing
395 eGFP-KNOLLE from its endogenous promoter in the absence and presence of Arabidopsis
396 CYCD3;1. The KNOLLE fusion protein was only detected when co-expressed with CYCD3;1 using
397 immunoblot analyses (Figure 7–figure supplement 1A) and labelled newly formed cell-division
398 planes (Figure 7–figure supplement 1B). This is consistent with previous reports showing that the
399 syntaxin KNOLLE accumulates only in dividing cells. We also confirmed the activation of the
400 Medicago KNOLLE promoter (pKNOLLE::GUS) in CDEL samples ectopically expressing
401 CYCD3;1 using a fluorometric GUS assay (Figure 7C). Next, we tested the impact of NF-YA1 on
402 the activity of promoters driving cell cycle-dependent gene transcription in the CDEL samples. While
403 NF-YA1 did not alter *GUS* expression when driven from the histone *H4* promoter (pH4::GUS) that
404 is active during DNA synthesis (Figure 7C-D; Yang et al., 1994), it significantly repressed
405 pKNOLLE::GUS activation (Figure 7E). This effect was fully abolished when using the mutated NF-
406 YA1^{mutDBD} variant (Figure 7E). Interestingly, the repressive effect of NF-YA1 was stronger compared
407 to the one observed when using a MYB3R transcriptional repressor from Medicago (Figure 7–figure
408 supplement 2A–B) known to halt the expression of late G2/M genes (Haga et al., 2007; Takahashi et
409 al., 2019). These results suggest that the NF-YA1 DNA-binding subunit prevents an unscheduled
410 entry into mitosis in de-differentiating leaf cells, despite the action of ectopically-expressed
411 CYCD3;1.

412 We then tested whether such effect could be observed at the cellular level in the CDEL system.
413 For this, we ectopically co-expressed non-fluorescently-tagged CYCD3;1 and NF-YA1 and
414 additionally transformed these leaves with fluorescently tagged Medicago H3.3 and KNOLLE

415 proteins, expressed from their native regulators (Figure 7–figure supplement 1B). While the
416 constitutive presence of NF-YA1 did not prevent cell division events *per se*, a significantly lower
417 proportion of transformed cells produced detectable levels of KNOLLE (Figure 7–figure supplement
418 1C), indicating that less pavement cells engaged in mitosis at the investigated experimental timepoint.
419 Cells visibly accumulating the KNOLLE protein still progressed through M-phase in the presence of
420 NF-YA1 (Figure 7–figure supplement 1B), although a smaller proportion of them fully completed
421 cell division at 64 hours when compared to the control samples (Figure 7–figure supplement 1D).
422 From these data we concluded that NF-YA1 is able to control mitotic entry in de-differentiating,
423 endoreduplicated cells at least in the CDEL system. Since symbiotically infected middle and inner
424 primordium layers, where *NF-YA1* expression was found to be confined in (Laporte et al., 2014; Liu
425 et al., 2019b), are comprised of endopolyploid cells (Figure 5C–E), we hypothesize that the Medicago
426 NF-YA1 protein might similarly modulate cell-cycle progression during symbiotic infections of
427 legume roots by rhizobia.

428

429 **DISCUSSION**

430 Failure to timely coordinate infection and organogenesis programs in the root cortex results in the
431 formation of poorly colonized nodules that are unable to support the plant's demand to obtain fixed
432 nitrogen (Guan et al., 2013; Laporte et al., 2014; Schiessl et al., 2023–pre-print). Here, we sought to
433 understand at cellular resolution, whether cell-cycle progression and cellular reprogramming are
434 altered in a spatially confined array of host cells that gain a time-limited stage of competence for
435 transcellular infection.

436 Our data support a model where dividing cells contributing to nodule formation, including
437 target cells for cortical infection, are polyploid and contain 4 copies (C) of each chromosome (Figure
438 5D–E). In Medicago, these 4C cells either pre-exist in the root cortex (Cebolla et al., 1999; Vinardell
439 et al., 2003; Carotenuto et al., 2019a; Carotenuto et al., 2019b) or arise from a single
440 endoreduplication round prior to their possible entry into cell division (Libbenga & Torrey, 1973).

441 As competent cells are crossed by a cortical infection thread or fully internalize bacteria and despite
442 being embedded into a proliferating tissue, they reach an 8C DNA content (Figure 6C and Figure 8)
443 but without committing to a subsequent cell division (Figure 4C–E). Rather, cells supporting
444 transcellular infections presumably use a cell-cycle GAP phase after DNA replication (*i.e.,* G2) and
445 extend such phase to remodel their histone H3 composition (Figure 2A–B and D). Finally, this
446 differentiation process and concomitant transcellular passage are accomplished within a single, last
447 cell-cycle round (Figure 2E; Otero et al., 2016). Here, and similar to infected root hairs (Breakspear
448 et al., 2014), a rapid switch to another endocycle is likely prevented as both G1- and S-phase markers
449 are kept low (Figure 4C). Taken together, these events control a cell-cycle progression state where
450 molecular players operate to ensure a successful transmission of rhizobia to the first nodule cells.
451

452 **Modulating endopolyploidy during rhizobial infections**

453 In line with findings from Arabidopsis reporting that a downregulation of *H3.1* gene expression and
454 a massive eviction process contribute to various differentiation programs in the male and female
455 gametes (Ingouff et al., 2010), the root meristem, the embryo (Otero et al., 2016) and the female
456 germline precursor (Lagana & Autran, 2020), we show that the genetic program enabling intracellular
457 infections of Medicago roots accesses the same mechanism (Figure 2A–B and Figure 2–figure
458 supplement 1C–E). Reciprocally, our data indicate that high H3.1 levels tend to be maintained in
459 infected cells with blocked or aborted infections (Figure 3A and C and Figure 3–figure supplement
460 1A–D). Furthermore, the nuclear enlargement in infected cells (Figure 2C) indicates profound
461 transcriptional reprogramming and activation of new gene regulatory networks as previously shown
462 to occur in LCO-treated (Knaack et al., 2022) or young symbiotic cells (*i.e.*, infected root hairs and
463 8C cells from mature nodules; Breakspear et al., 2014; Nagymihály et al., 2017; Liu et al., 2019a).
464 We expanded the latter view by showing that tetraploid cortical cells crossed by an infection thread
465 also reach a presumable 8C DNA content (Figure 6C). As reported for growing cell types in
466 Arabidopsis (Bhosale et al., 2018), such alteration in endopolyploidy might support, among others,

467 changes in cell wall compositions, which have also recently been demonstrated to occur specifically
468 around infected cells in Medicago (Su et al., 2023; Gaudioso-Pedraza et al., 2018). In the determinate
469 nodulator *L. japonicus*, polyploidization of early nodule cells might be controlled by *VAGRANT*
470 *INFECTION THREAD 1* (*VAG1*), a putative component of DNA topoisomerase VI (topo VI)
471 complex, as cortical cells with reduced ploidy levels cannot be infected in the *vag1* mutant (Suzaki
472 et al., 2014).

473 Interestingly, but different to infections by mycorrhizal fungi where repetitive rounds of
474 endoreduplication occur (Figure 1C; Russo & Genre, 2021) and support fungal colonization
475 (Carotenuto et al., 2019a; Carotenuto et al., 2019b), markedly reduced histone H3.1 contents in cells
476 maintaining rhizobial infections in the root cortex up to the first recipient cells in nodule primordia
477 indicate reduced endocycling rates (Figure 2D-E; Otero et al., 2016). Such attenuation of cell-cycle
478 progression together with decreased transcript levels of mitotic cyclins were shown to occur in
479 budding yeast and Arabidopsis (Negishi et al., 2016; Gigli-Bisceglia et al., 2018) following the
480 activation of a cell-wall integrity (CWI) checkpoint. More recently, Ma and colleagues proposed a
481 scenario where the CWI kinase THESEUS1 (THE1), with a related gene being induced in infected
482 root hairs (Breakspear et al., 2014; Liu et al., 2019a), triggers cell wall stiffening as a response to
483 endoreduplication attenuation (Ma et al., 2022).

484

485 **A G2-phase arrest and attenuated endoreduplication as a plausible context for cortical**
486 **infections**

487 Reaching and staying in a pre-mitotic stage has been proposed to facilitate the long-distance
488 progression of infection threads in legume species forming so-called cortical, pre-infection threads
489 (PITs) (Yang et al., 1994; Timmers et al., 1999; Van Spronsen et al., 2001; Foucher & Kondorosi,
490 2000). These structures resemble the onset of a cell division plane that requires the formation of a
491 cortical division zone (Smertenko et al., 2018), which is established from late S- through G2 phases
492 (Costa et al., 2016; Schaefer et al., 2017). Interestingly, this cell-cycle progression window coincides

493 with the one we observed in infected cortical cells (Figure 2A–E and Figure 4A-C). In addition, the
494 existence of pre-mitotic and G2-arrested cortical cells on the infection thread trajectory is in line with
495 a recent report showing that a rhizobium-induced mitotic module, comprising an α-Aurora kinase
496 gene and its MYB3R transcriptional activator, supports endosymbiotic infection in Medicago (Gao
497 et al., 2022). Interestingly though, overexpression of the activator-type *MYB3R1* gene resulted in the
498 formation of abnormally bulbous or branched infection threads (Gao et al., 2022). These data
499 emphasize the need to balance the activity of transcriptional regulators driving mitosis and
500 cytokinesis in infected cells.

501 In summary, we hypothesize that endocycle suppression after a round of DNA replication
502 (Breakspear et al., 2014) and exiting the cell-cycle from the G2-phase might therefore create a
503 permissive, yet controlled state for cortical infection thread progression where polarization and cell-
504 wall remodelling factors specialized for intracellular infection (Lace et al., 2023; Su et al., 2023) act
505 in a defined cell-cycle window to sustain infection thread growth and guidance across cortical layers.
506

507 **Endopolyploidization following cytokinin perception: a legume innovation?**

508 Using the centromeric histone H3 (CENH3) fluorescent reporter enabled us to assess chromosome
509 numbers, the progression through the G2 phase (Figure 6–figure supplement 1A–B; Lermontova et
510 al., 2006) and to clearly identify diploid and polyploid cells (Figure 5 B and E; De Storme et al.,
511 2016). Combining CENH3 patterns with the histone H3.3 marker showed that somatic cortical cells
512 giving rise to indeterminate Medicago root nodules are mainly tetraploid, which is consistent with
513 previous observations (Wipf & Cooper, 1938; Torrey & Barrios, 1969). Furthermore, our imaging
514 data indicate that dividing endopolyploid cells are homogenously maintained in the nodule tissue
515 (Figure 5–figure supplement 2B–C). This suggests that tetraploidization is an important feature for
516 nodule fitness and infectability as it may enable processes such as the required integration of many
517 contextual stimuli (*e.g.* bacterial signals) (Doyle & Coate, 2019; Russo & Genre, 2021), the
518 coordination of controlled organogenesis and a greater cellular adaptability to hypoxic environments

519 as also suggested for human tumour cells (Yant & Bomblies, 2015). Furthermore, our findings point
520 towards tetraploidization of cortical cells being a hallmark for nodule identity as pericycle cells in
521 nodule or lateral root primordia remain strictly diploid (Figure 5E and Figure 5–figure supplement
522 2C). Interestingly, when dissected and cultured in suspension, cortical cells from the susceptible zone
523 of pea roots entered cell divisions as tetraploid cells only when cytokinin (kinetin) was applied in
524 addition to auxin (2,4-D; Libbenga & Torrey, 1973). This is particularly interesting since a specific
525 cortical response to cytokinin, an auxin/cytokinin interplay and subsequent cellular proliferations in
526 the root cortex appear to be a legume innovation (Guan et al., 2013; Gauthier-Coles et al., 2019).
527

528 **NF-YA1, possible intermediary between intracellular infection and cell-cycle control**

529 While this and other reports have shed light onto cell-cycle patterns during rhizobial infections in
530 roots and nodules, genetic factors coordinating cell-cycle progression and intracellular infections
531 remained enigmatic. Using the heterologous CDEL system (Xu et al., 2020) has enabled us to test the
532 impact of at least one of the potential candidates, the symbiotic transcription factor NF-YA1, on cell
533 cycle-dependent activities in a de-differentiating cellular population. Expression of NF-YA1 in this
534 system did not prevent cells from passing through S-phase (Figure 7D). But, while the activated cells
535 (as indicated by the induction of the KNOLLE reporter) still engage in mitosis and eventually divide
536 (Figure 7–figure supplement 1B), significantly fewer transformed cells promoted the expression of
537 this G2/M marker at our experimental timepoints (Figure 7E and Figure 7–figure supplement 1C)
538 These results strongly suggest that, in the CDEL system, NF-YA1 negatively regulates the entry into
539 mitosis despite the presence of CYCD3;1. The latter has been shown to promote mitotic cycles and
540 to restrain differentiation and endoreduplication when accumulated in shoot tissues (Schnittger et al.,
541 2002; Dewitte et al., 2003). Our observations are also consistent with findings in mammalian cells,
542 where the NF-Y trimer mediates the repression of key mitotic genes in complex with the WT p53
543 protein (Imbriano et al., 2005; Di Agostino et al., 2006) during a G2 arrest induced by genotoxic
544 stress (Manni et al., 2001). A link to DNA damage control, potentially arising when endoreduplicated

545 pavement cells are pushed back into a chromosome segregation cycle, seems likely in the CDEL
546 system. However, whether NF-YA1 similarly monitors cell division activity in polyploid nodule
547 primordium cells (Figure 5E) and controls the G2/M transition along the infection thread trajectory
548 and in intracellularly colonized nodules (Figure 6B) are aspects that need to be addressed
549 independently.
550
551 In summary, we propose that a local control of cell-cycle activity and a cell-cycle exit decision along
552 the infection thread trajectory provide a window of cellular competence for cortical infections to
553 progress down to the nodule primordium niche in Medicago. We demonstrated that the cell division
554 and differentiation potentials are controlled in a spatially confined cell-file in the root cortex. We also
555 show that post-replicative, tetraploid cells reaching an 8C DNA content are optimal for intracellular
556 infection. Consequently, it is tempting to hypothesize that exactly these cells comprise a highly
557 specific transcriptional and regulatory landscape that ultimately defines the molecular susceptibility
558 state for intracellular infection competence.
559
560
561 **MATERIALS AND METHODS**
562 **Plant materials and growth conditions**
563 The Medicago wild-type (WT) ecotype A17, cultivar Jemalong was used in this study. The *daphne-*
564 *like* (FN8113) and *nf-ya1-1*mutant lines have been described previously (J. Liu et al., 2019; Laporte
565 et al., 2014). Seeds from the *daphne-like* mutant were kindly provided by Rene Geurts (Laboratory
566 of Molecular Biology, Wageningen University, The Netherlands).
567 Seeds were scarified by covering them with sulfuric acid (H_2SO_4) 96% for 8 minutes and washed 6
568 times with sterile tap water. After surface sterilization with a bleach solution (1.2% sodium
569 hypochlorite, NaClO and 0.1% sodium dodecyl sulfate, SDS) for 1 min, the 6 washing steps were

570 repeated and seeds were sown on 1% (w/v) agar plates. Seeds were then stratified at 4 °C for 5 days
571 in the dark before being germinated at 22 °C in the dark for 16 h.
572
573 **Hairy root transformation**
574 Composite *Medicago* plants were generated with transgenic hairy roots as previously described
575 (Boisson-Dernier et al., 2001). *Agrobacterium rhizogenes* ARquaI cells carrying the desired binary
576 vector were cultured in liquid LB medium containing appropriate antibiotics at 28 °C, shaking
577 overnight. Three hundred µl of the culture (OD 600 nm: 0.5-0.7) were plated on solid LB medium
578 with corresponding antibiotics and incubated at 28 °C for 2 days. Plants were prepared by removing
579 the seed coat from germinated seedlings and about 5 mm of the root tip region was removed before
580 the cut site was dipped into the solid *A. rhizogenes* culture. Up to 25 inoculated seedlings were placed
581 on solid Fahräeus medium supplemented with 0.5 mM NH_4NO_3. Transformed seedlings were then
582 grown vertically in a climate chamber at 21° C for 3 days in the dark. After another 4 days at 21 °C
583 (16 h light/8 h dark, 35 µmol m^{-2} s^{-1} light intensity), with only the roots protected from illumination,
584 composite plants were transferred to fresh solid Fahräeus plates (0.5 mM NH_4NO_3) and grown for 10
585 days at 22 °C following the same photoperiod. Transgenic roots were visualized based on the
586 fluorescence emitted by nuclear markers (*M.t.* pH3.3::H3.3-mCherry; *A.t.* pH3.1::H3.1-mCherry;
587 pLjUbi::NLS-2xmCherry) using an AXIO Zoom.V16 stereomicroscope (Zeiss). Un-transformed
588 roots were removed and the composite plants were transferred in pots (7x7x8 cm) containing a
589 mixture of quartz sand and vermiculite (1:1 v/v) equilibrated with 25 ml of a ¼ Hoagland solution
590 (0.1 mM KNH3). After 4 days of acclimation (16/8 h light/dark photoperiod, 24 °C temperature, 60%
591 humidity and 70-90 µmol m-2 s-1 light intensity), plants were subjected to rhizobial inoculation.
592 For this, *S. meliloti* (Sm2011) strains producing mCherry or GFP were grown on solid TY medium
593 containing 10 µg/ml tetracycline for 2 days at 28 °C. A single colony was used as an inoculum and
594 bacteria were grown in liquid TY medium containing the antibiotic at 28 °C, shaking for 2 days. Cells
595 were centrifuged for 8 min at 2205 g, washed once with liquid Fahräeus medium and finally

596 resuspended into the same medium to reach an OD 600 nm of 0.0015. Five ml of this bacterial
597 suspension were applied to each composite plant. Pots were watered twice a week with tap water and
598 fertilized with a ¼ Hoagland solution (0.1mM KNH3) once a week. Transgenic roots were harvested
599 at different timepoints (8 to 14 days) for tissue fixation, clearing and deep tissue imaging by confocal
600 microscopy.
601
602 **Construct design**
603 For expressing the canonical (*H3.1*) and replacement (*H3.3*) histone genes of *M. truncatula*
604 (Medicago), genomic fragments containing the promoters (*H3.1*: 2623 bp; *H3.1* (2): 2580 bp; *H3.3*:
605 2739 bp) and open reading frames (ORF) except the termination codon were used. The pH4::GUS
606 reporter used in quantitative fluorometric assays comprised a 2080 bp fragment of the promoter.
607 Expression of the centromeric histone (*CENH3*) gene (coding sequence) was driven by a tentative
608 promoter comprising 1000 bp upstream of the start codon. Transcriptional KNOLLE reporters were
609 driven by a 2325 bp-long fragment of the *KNOLLE* promoter. The core pentamer of all three mitosis-
610 specific activator (MSA) cis-elements (AACGG) within the *KNOLLE* promoter was mutated by
611 changing two bases (ATTGG) according to Ito et al., 2001. The *KNOLLE* genomic sequence was
612 used to build the translational reporter (pKNOLLE::eGFP-KNOLLE). For Medicago NF-YA1, the
613 genomic sequence was used and the NF-YA1^{mutDBD} variant was created by replacing the conserved
614 RGC amino acid residues (positions 213-215) by an AAA triplet according to Laloum et al., 2014.
615 For the repressor-type *MYB3R* transcription factor, the coding sequence (CDS) was used. All
616 Medicago sequence information was obtained from the Mt4.0v1 genome through Phytozome.
617 The *A. thaliana* (Arabidopsis) pCYCB1;2::N-CYCB1;2-NLS-3xVenus reporter construct was
618 designed according to Trolet et al., 2019 and included a genomic fragment (AT5G06150) of 1929 bp,
619 comprising 1090 bp of promoter sequence, the 5' untranslated region and 839 bp from the ORF
620 including the first intron. Addition of 2 bases (GG for Gly) at the 3' end of this genomic fragment
621 enabled the production of the N-terminal CYCB1;2 domain (including the destruction box [D-box]

622 motif) fused in-frame to a triple-Venus nuclear reporter (Binder et al., 2014; Nadzieja et al., 2019).
623 The CYCB1;1 N-terminal (D-box) domain was produced from a genomic fragment (AT4G37490) of
624 713 bp including the first 2 introns (nucleotides [nts] 41-308 and 488-584) and 129 bp of the third
625 exon (nts 585-713). This module was fused in-frame to a triple-Venus nuclear FP to generate a
626 destabilized version of the fluorescent reporter. The CYCD3;1 (AT4G34160) CDS was placed under
627 control of the cauliflower mosaic virus (CaMV) 35S promoter (426 bp) and fused in frame to a 3xHA
628 module to build the p35S::CYCD3;1-HA construct. Arabidopsis sequence data can be found on
629 Phytozome (*Arabidopsis thaliana* TAIR10 annotation version). To produce the C-terminally
630 truncated, hyperactive version of the *N. tabacum* MybA2 transcriptional activator (pLjUbi::eGFP-
631 NtMybA2ΔC), the CDS (GenBank accession: AB056123.1) coding for the first 630 amino acid
632 residues was used (Araki et al., 2004). The GoldenBraid PlaCCI transformation plasmid was kindly
633 provided by Bénédicte Desvoyes and Crisanto Gutierrez (Centro de Biologia Molecular Severo
634 Ochoa, CSIC-UAM, Madrid, Spain).

635 **Construct production using the Golden Gate cloning system**

636 The Golden Gate modular cloning (MoClo) system was used to generate binary plasmids for
637 transgene expression in plant cells (Weber et al., 2011). Promoter, genomic and coding sequences
638 were synthetized and cloned into pMS-RQ (GeneArt, Thermo Fisher Scientific, Regensburg,
639 Germany). Level 0 (L0) functional modules used in this study are held for distribution in the ENSA
640 project collection (https://www.ensa.ac.uk/). Details of the L1 expression cassettes and L2 binary
641 vector composition, including used promoters, genetically encoded fluorescent proteins (stable or
642 short-lived) or epitope tags and the accession numbers for requesting constructs, are provided in a
643 supplementary file (Table S1). One-pot reactions using the Type IIS restriction enzymes BsaI-HFv2
644 (R3733S) and BpiI / BbsI-HF (R3539S) and the T4 DNA ligase (M0202S), all from New England
645 BioLabs (Frankfurt am Main, Germany), were assembled according to Binder et al., 2014. Cut-
646 ligation reactions were cycled 50 times between 37 °C for 2 min and 25 °C for 5 min, followed by 5

647 min at 50 °C and 5 min at 80 °C. Five µl of the reaction were transformed into *E. coli* Stbl3 (for L1
648 and L2 plasmids carrying histone H3.1 or H3.3 expression cassettes) or TOP10.

649

650 **Root colonization by *R. irregularis***

651 Following excision of un-transformed roots, composite Medicago plants were transferred to chive (*A.*
652 *schoenoprasum*) nurse pot (9 x 9 cm) systems containing *R. irregularis* (DAOM 197198, sterile spore
653 inoculum from Agronutrition, France) set up according to Demchenko et al., 2004 (4 plants x pot).
654 Each pot was covered with a transparent plastic bag (20 x 30 cm) for two days to keep plants in
655 moisturized conditions. Plants were grown in a controlled environment chamber at 24 °C with a 16/8
656 hour light/dark photoperiod, with each pot being watered every second or third day with 50 ml
657 deionized water and fertilized once per week with 50 ml ¼ Hoagland medium. After 7 to 15 days of
658 co-culturing, composite plants were harvested and excised transgenic roots were subjected to fixation,
659 clearing and Calcofluor White staining prior to imaging.

660

661 **Clearing and staining of the root material**

662 The presence of all expected fluorescent reporters was verified in the meristematic region using an
663 AXIO Zoom.V16 stereomicroscope (Zeiss) before further analyzing the transgenic roots. Fixation,
664 clearing and cell-wall counter-staining procedures were performed according to Ursache et al., 2018.
665 Briefly, transformed roots were isolated and fixed in a freshly prepared 4% paraformaldehyde (PFA)
666 solution in 1x phosphate-buffered saline (PBS), infiltrated under vacuum for 15 min and then gently
667 agitated for 60-120 min at room temperature in the dark. After 2 washes in 1x PBS, roots were
668 transferred to the clearing (ClearSee) solution and incubated 7 to 10 days with gentle shaking,
669 changing the ClearSee solution every 2 days. Prior to imaging, roots were stained with 0.1%
670 Calcofluor White in ClearSee for 1 h, before being rinsed once and washed in the clearing solution

671 for 30 min. Calcofluor White was imaged using a 405 nm laser diode excitation source and a 425–
672 475 nm detection window.
673
674 **Nodule sections**
675 To assess the localization pattern of H3.1 and H3.3 histone variants across different nodule zones,
676 composite plants were generated by hairy root transformation as described above. Nodules were
677 harvested 35 to 40 days after inoculation in open pots and fixed in 4% (w/v) PFA in 1x PBS, under
678 vacuum treatment for 15 min and then gently agitated for 45 min at room temperature. The fixed
679 samples were embedded in 6% (w/v) low melting temperature agarose (Biozym) and longitudinal
680 sections (70 µm thickness) were obtained using a VT1000S vibratome microtome (Leica Biosystems,
681 Mannheim, Germany).
682
683 **Fluorescent reporter imaging by Confocal Laser-Scanning Microscopy (CLSM)**
684 Imaging of plant material (*i.e.,* nodule semi-thin sections and cleared root samples) was performed
685 using a TCS SP8 confocal microscope (Leica Microsystems, Mannheim, Germany) controlled by the
686 LAS X v3 software. Images were acquired with a 20x/0.75 or a 40x/1.10 (HC PL APO CS2) water
687 immersion objective. Genetically encoded FPs were excited with an argon laser or a White Light
688 Laser (WLL) source. Emitted photons were collected using hybrid detectors (HyDs). eCFP was
689 excited with an argon laser line at 458 nm and the emission was detected at 470-510 nm. All other
690 FPs were excited with WLL excitation (ex) lines and emissions (em) were detected according to the
691 following settings: eGFP = 488 nm (ex) / 500-550 nm (em); YFP = 515 nm (ex) / 525-586 nm (em);
692 mCitrine and Venus = 515 nm (ex) / 525-550 (em); mCherry: 561 or 587 nm (ex) / 600-650 or 620-
693 650 nm (em).
694

695 **Image analysis and quantification of nuclear fluorescent signals**

696 All images were processed and analyzed using the Fiji/ImageJ open-source software (Schindelin et
697 al., 2012). Image files were used to create figure panels through the FigureJ plugin (Mutterer & Zinck,
698 2013). If not indicated differently, 2D maximum intensity projections of z-stacks are presented in the
699 figures. All quantitative measurements were performed on single focal planes and single channels
700 from un-processed z-stacks, acquired from fully transformed Medicago roots. The Fire lookup table
701 (LUT) was applied to facilitate the visualization of low-intensity pixels. Nuclear areas were measured
702 at the equatorial plane using the freehand selection tool, on channels displaying the signal from
703 chromatin-associated proteins (*i.e.*, H3.1 or H3.3-FP fusions). H3.1-eGFP levels were quantified in
704 the nucleus of infected cells (IC) and of directly adjacent, neighbouring cells (NC) present on the
705 same z-stack in the same cortical layer. For this, an outline was manually drawn around each nucleus
706 at the equatorial plane and area, integrated density and mean gray values were measured. Three oval
707 selections were drawn adjacent to all measured nuclei to be used for normalization against
708 background fluorescence. The corrected total nuclear fluorescence (CTNF) = integrated density –
709 (area of selected nucleus × mean fluorescence of background readings) was calculated according to
710 McCloy et al., 2014 using Excel. The number of mCitrine-CENH3 signals in individual nuclei and
711 mitotic figures was manually determined across image stacks using the multi-point tool. The length
712 of CENH3 fluorescent doublets was measured between the 2 most distant pixels using the straight-
713 line tool.

714

715 **Transient expression in *N. benthamiana* leaves**

716 Four to 5-weeks old tobacco (*N. benthamiana*) plants were transiently transformed with *A. rhizogenes*
717 (ARqua1) cells carrying the construct of interest. The first, second and third fully expanded true
718 leaves were used for infiltration experiments using needle-less syringes. Agrobacteria were
719 resuspended in a MES/KOH infiltration buffer (10 mM, pH 5.6) supplemented with 10 mM $MgCl_2$
720 and 150 µM acetosyringone. Bacterial cultures used for co-transformations were diluted to a final OD

721 600 nm of 0.1 for each construct. *A. tumefaciens* (GV3101) cells producing the p19 silencing
722 suppressor (Silhavy et al., 2002), were systematically included at a final OD 600 nm of 0.05. Upon
723 infiltration, plants were further grown for 64 to 72 h before harvesting leaf samples with a biopsy
724 puncher (4 mm diameter) in the distal half of fully infiltrated leaves. Four to 5 leaf discs were either
725 mounted in sterile tap water and imaged with a confocal microscope, or 10 leaf disks were frozen in
726 liquid nitrogen prior to *in vitro* transactivation assays.
727
728 **Cell division-enabled leaf system (CDELS)**
729 To foster differentiated pavement cells to enter the cell division cycle, non-fluorescently-tagged
730 Arabidopsis CYCD3;1 was expressed under control of the CaMV 35S promoter by Agrobacterium
731 infiltration (Xu et al., 2020). The p35S::CYCD3;1-HA construct was co-transformed with binary
732 vectors allowing native expression of cell cycle regulated-reporters (pH4::GUS, pKNOLLE::GUS,
733 pKNOLLE::eGFP-KNOLLE) and constitutive expression of transcription factors (NF-YA1, NF-
734 YA1^{mutDBD}) from Medicago. All plasmids used in the experiments involving the CDEL system are
735 listed in Table S1. Transformed leaves homogenously expressing nuclear transformation markers
736 included on the corresponding binary vectors were selected using an AXIO Imager.M2m ApoTome.2
737 light microscope (Zeiss). The activity of HA-tagged CYCD3;1 was verified by the presence of at
738 least one mitotic figure with chromosomes labeled by H3.3-mCherry before harvesting.
739
740 **Immunoblot analyses**
741 To detect proteins transiently produced in the CDEL samples, 3 discs from 64 h post-infiltration
742 leaves were frozen in liquid nitrogen and ground to powder using a Tissue Lyser MM300 (Retsch).
743 The powder was resuspended in 120 µl of 2x loading buffer and heated for 8 min at 95 °C. Equal
744 volumes of samples were loaded and separated by 10% SDS-polyacrylamide gel electrophoresis
745 (PAGE) at constant voltage (80V). Proteins were transferred to a PVDF membrane (0.2 µm pore size)
746 using the Trans-Blot® Turbo™ semi-dry transfer system (7 min mixed MW MIDI program) (Bio-

747 Rad). After blocking in a 2.5% (w/v) milk/TBST solution for 1 h at RT, transferred membranes were
748 hybridized overnight at 4 °C with the following primary antibodies: anti-GFP (632381, Takara)
749 (1/5000); anti-DsRed (632496, Takara) (1/5000); peroxidase-conjugated anti-HA (clone 3F10,
750 12013819001, Roche) (1/2000); anti-FLAG M2 (F3165, Sigma-Aldrich) (1/2000). Membranes were
751 washed and incubated 1 h at RT with peroxidase-conjugated secondary antibodies (anti-mouse, A
752 4416; anti-rabbit, A 6154; Sigma-Aldrich) (1/2000). Immunoblotted proteins were detected using the
753 Clarity Western ECL Substrate (Bio-Rad). Digital images were acquired using an ECL ChemoCam
754 Imager (Intas Science imaging) with exposures stopped before saturation.
755
756 **Transactivation and quantitative fluorometric GUS assays**
757 *N. benthamiana* leaf samples used for GUS fluorometric assays were harvested 72 h post-infiltration.
758 The same number of plasmids was used for all co-transformation experiments. A construct driving
759 the accumulation of a nuclear FP (proH3.1::NLS:3xVenus) was included in the absence of exogenous
760 transcription factors. Ten leaf discs per transformed leaf were frozen in liquid nitrogen inside a Safe
761 Seal Micro tube containing a stainless-steel bead (5 mm diameter). Samples were ground twice for
762 30 s (28/s frequency) using a Tissue Lyser MM300 (Retsch) and the powder was resuspended in 400
763 µl of cold GUS extraction buffer (50 mM $NaHPO_4$, pH 7.0, 1 mM EDTA, 10 mM DTT, 0.05% [v/v]
764 Triton X-100 and 1x Protease Inhibitor Cocktail [Roche]). Crude leaf extracts were incubated for 2 h
765 at 4 °C on a turning wheel and centrifuged at 16.900 g for 5 min at 4 °C. Ten µl of the supernatant
766 were used to determine protein concentrations by the dye-binding Bradford assay (Bio-Rad). Twenty-
767 five µg of total proteins in a final volume of 100 µl were pipetted into a white 96 well plate (Greiner
768 Bio-One) before the addition of 200 µl of GUS reaction buffer (50 mM $NaHPO_4$, pH 7.0, 1 mM
769 EDTA, 1% [v/v] Triton X-100 and 0.5 mM 4-Methylumbelliferyl-β-D-glucuronide [4-MUG] [Carl
770 Roth]). After 10 min of incubation at 37 °C in the dark, the fluorescence emitted by GUS-mediated
771 hydrolysis of 4-MUG into 4-Methylumbelliferone (4-MU) was measured using a microplate reader
772 (POLARstar Omega, BMG LABTECH). Fluorescence was recorded at 360 nm excitation and 460

773 nm emission filter (gain 500, 20 flashes per well) every 5 min over a time period of 130–180 min.
774 Samples were run in technical triplicates and blank measurements (100 µl extraction buffer + 200 µl
775 reaction buffer) were performed to correct for any nonenzymatic hydrolysis of 4-MUG. Corrected
776 GUS activities (4-MU fluorescence units [FU] min^{-1}) were calculated as: $A_{GUS} = \Delta F / \Delta t = (F1-F0) /$
777 Δt where ΔF is the difference in fluorescence intensities measured in the linear range of the
778 fluorescence curves over a 15 min period of time (Δt). Values were normalized to 1 µg of protein
779 content by using the protein concentration determined via Bradford assay. Two to 5 independent
780 experiments were performed with at least 3 leaves from 2 different plants analyzed.
781
782 **Data visualization and statistical analysis**
783 Alignment of multiple protein sequences was performed using Jalview (version 2.11.2.6) (Procter et
784 al., 2021). Statistical analyses and generation of figures were performed using the GraphPad Prism
785 software (version 9.5.1) (GraphPad Software Inc.). Normal distribution of data was tested using the
786 Shapiro-Wilk and Kolmogorov-Smirnov normality tests. A Brown-Forsythe and Welch ANOVA test
787 followed by Dunnett's multiple T3 comparisons or an unpaired t-test with Welch's correction were
788 applied as parametric tests. Kruskal-Wallis followed by Dunn's multiple comparisons or Mann-
789 Whitney tests were applied as non-parametric tests. Boxes in the box-and-whiskers plots extend from
790 the 25th to 75th percentiles and whiskers range from the smallest to the largest values. Middle
791 horizontal lines are plotted at the median. Sample size n, statistical tests and significance levels are
792 provided in the figure legends. Source data and results of the statistical analyses are provided as
793 supplement files associated to the corresponding figure.
794
795 ***M. truncatula* gene identifiers**
796 Accession numbers for the *M. truncatula* (Medicago) genes used in this study are provided from the
797 following genome portals, Phytozome (Mt4.0v1 version; https://phytozome-next.jgi.doe.gov/;
798 Goodstein et al., 2012) and / Medicago truncatula A17 r5.0 (A17 r5.1.9 version;

799 https://medicago.toulouse.inra.fr/MtrunA17r5.0-ANR/; Pecrix et al., 2018), respectively: *H3.1* (1)
800 (Medtr8g092720 / MtrunA17_Chr8g0383781); *H3.1* (2) (Medtr8g103245 /
801 MtrunA17_Chr8g0390361); *H3.3* (Medtr4g097175 / MtrunA17_Chr4g0054161); *H4*
802 (Medtr7g099610 / MtrunA17_Chr7g0262791); *KNOLLE* (Medtr5g012010 /
803 MtrunA17_Chr5g0398891); *CENH3* (Medtr8g027840 / MtrunA17_Chr8g0347231); repressor-type
804 *MYB3R* (Medtr7g061330 / MtrunA17_Chr7g0238631); *NF-YA1* (Medtr1g056530 /
805 MtrunA17_Chr1g0177091).
806

807 **DATA AVAILABILITY STATEMENT**

808 All data generated and analyzed during this study are included in the manuscript and supporting files.
809 All sequences have been obtained from publicly available repositories and indicated in the Materials
810 and Methods section.
811

812 **MATERIALS AVAILABILITY STATEMENT**

813 All material generated within this study can be obtained from the corresponding authors upon request.
814 Plasmids obtained from other laboratories as indicated in the respective sections need to be requested
815 from the original producer.
816

817 **ACKNOWLEDGEMENTS**

818 We would like to thank the entire team for the constant and fruitful input into the project and
819 especially Eija Schulze and Carmen Schubert for their excellent experimental support. Furthermore,
820 we greatly appreciated the technical help of Zenglin Li and Philipp Schwenk (University of Freiburg,
821 Germany) on GUS fluorometric assays. Jean Keller (LRSV Toulouse, France now Max-Planck
822 Institute for Chemical Ecology, Jena, Germany) conducted a comprehensive phylogeny on MYB3R,
823 MEME and FIMO searches on MSA motifs. Katharina Schiessl (University of Cambridge, UK)
824 provided the *nf-ya1-1* seeds and fruitful comments throughout the project. We also thank the staff of

the Life Imaging Center (LIC) in the Hilde Mangold House (HMH) of the Albert-Ludwigs-University of Freiburg for the help with their confocal microscopy resources, and the excellent support in image recording. The microscopes are operated by the Microscopy and Image Analysis Platform (MIAP) and the Life Imaging Center (LIC), Freiburg.

FUNDING

Engineering Nitrogen Symbiosis for Africa (ENSA) project currently supported through a grant to the University of Cambridge by the Bill & Melinda Gates Foundation (OPP1172165) and UK government's Department for International Development (DFID) (TO)

Deutsche Forschungsgemeinschaft (DFG, German Research Foundation) 431626755 (TO)

DFG under Germany's Excellence Strategy grant CIBSS – EXC-2189 – Project ID 39093984 (TO)

China Scholarship Council (CSC) grant 201708080016 (CS)

DFG project number 414136422 (CLSM; TO), DFG project number 426849454 (TEM; TO)

AUTHOR CONTRIBUTIONS

Conceptualization: MB, TL, TO; Investigation: MB, BL, NZ, CS, SE, PK, JS, FAD; Writing – Original Draft: MB, TO; Writing –Review & Editing: MB, BL, NZ, CS, SE, PK, JS, FAD, TL, TO; Supervision: MB, TL, TO; Project administration: TO; Funding Acquisition: TL, TO

REFERENCES

Araki, S., Ito, M., Soyano, T., Nishihama, R., & Machida, Y. (2004). Mitotic cyclins stimulate the activity of c-Myb-like factors for transactivation of G2/M phase-specific genes in tobacco. *J Biol Chem*, *279*(31), 32979-32988. https://doi.org/10.1074/jbc.M403171200

Bardetti, P., Castanheira, S. M., Valerius, O., Braus, G. H., & Perez-Martin, J. (2019). Cytoplasmic retention and degradation of a mitotic inducer enable plant infection by a pathogenic fungus. *Elife*, *8*. https://doi.org/10.7554/eLife.48943

851 Baudin, M., Laloum, T., Lepage, A., Ripodas, C., Ariel, F., Frances, L., Crespi, M., Gamas, P.,
852 Blanco, F. A., Zanetti, M. E., de Carvalho-Niebel, F., & Niebel, A. (2015). A Phylogenetically
853 Conserved Group of Nuclear Factor-Y Transcription Factors Interact to Control Nodulation
854 in Legumes. *Plant Physiol*, *169*(4), 2761-2773. https://doi.org/10.1104/pp.15.01144
855 Berckmans, B., & De Veylder, L. (2009). Transcriptional control of the cell cycle. *Curr Opin Plant*
856 *Biol*, *12*(5), 599-605. https://doi.org/10.1016/j.pbi.2009.07.005
857 Bhosale, R., Boudolf, V., Cuevas, F., Lu, R., Eekhout, T., Hu, Z., Van Isterdael, G., Lambert, G. M.,
858 Xu, F., Nowack, M. K., Smith, R. S., Vercauteren, I., De Rycke, R., Storme, V., Beeckman,
859 T., Larkin, J. C., Kremer, A., Hofte, H., Galbraith, D. W., … De Veylder, L. (2018). A
860 Spatiotemporal DNA Endoploidy Map of the Arabidopsis Root Reveals Roles for the
861 Endocycle in Root Development and Stress Adaptation. *Plant Cell*, *30*(10), 2330-2351.
862 https://doi.org/10.1105/tpc.17.00983
863 Binder, A., Lambert, J., Morbitzer, R., Popp, C., Ott, T., Lahaye, T., & Parniske, M. (2014). A
864 modular plasmid assembly kit for multigene expression, gene silencing and silencing rescue
865 in plants. *PLoS One*, *9*(2), e88218. https://doi.org/10.1371/journal.pone.0088218
866 Boisson-Dernier, A., Chabaud, M., Garcia, F., Becard, G., Rosenberg, C., & Barker, D. G. (2001).
867 Agrobacterium rhizogenes-transformed roots of Medicago truncatula for the study of
868 nitrogen-fixing and endomycorrhizal symbiotic associations. *Mol Plant Microbe Interact*,
869 *14*(6), 695-700. https://doi.org/10.1094/MPMI.2001.14.6.695
870 Bolognese, F., Wasner, M., Dohna, C. L., Gurtner, A., Ronchi, A., Muller, H., Manni, I., Mossner,
871 J., Piaggio, G., Mantovani, R., & Engeland, K. (1999). The cyclin B2 promoter depends on
872 NF-Y, a trimer whose CCAAT-binding activity is cell-cycle regulated. *Oncogene*, *18*(10),
873 1845-1853. https://doi.org/10.1038/sj.onc.1202494
874 Breakspear, A., Liu, C., Roy, S., Stacey, N., Rogers, C., Trick, M., Morieri, G., Mysore, K. S., Wen,
875 J., Oldroyd, G. E., Downie, J. A., & Murray, J. D. (2014). The root hair « infectome » of
876 Medicago truncatula uncovers changes in cell cycle genes and reveals a requirement for Auxin
877 signaling in rhizobial infection. *Plant Cell*, *26*(12), 4680-4701.
878 https://doi.org/10.1105/tpc.114.133496
879 Bu, F., Rutten, L., Roswanjaya, Y. P., Kulikova, O., Rodriguez-Franco, M., Ott, T., Bisseling, T.,
880 van Zeijl, A., & Geurts, R. (2020). Mutant analysis in the nonlegume Parasponia andersonii
881 identifies NIN and NF-YA1 transcription factors as a core genetic network in nitrogen-fixing
882 nodule symbioses. *New Phytol*, *226*(2), 541-554. https://doi.org/10.1111/nph.16386

883 Carotenuto, G., Sciascia, I., Oddi, L., Volpe, V., & Genre, A. (2019b). Size matters : Three methods
884 for estimating nuclear size in mycorrhizal roots of Medicago truncatula by image analysis.
885 *BMC Plant Biol*, *19*(1), 180. https://doi.org/10.1186/s12870-019-1791-1
886 Carotenuto, G., Volpe, V., Russo, G., Politi, M., Sciascia, I., de Almeida-Engler, J., & Genre, A.
887 (2019a). Local endoreduplication as a feature of intracellular fungal accommodation in
888 arbuscular mycorrhizas. *New Phytol*, *223*(1), 430-446. https://doi.org/10.1111/nph.15763
889 Carrere, S., Verdier, J., & Gamas, P. (2021). MtExpress, a Comprehensive and Curated RNAseq-
890 based Gene Expression Atlas for the Model Legume Medicago truncatula. *Plant Cell Physiol*,
891 *62*(9), 1494-1500. https://doi.org/10.1093/pcp/pcab110
892 Cathebras, C., Gong, X., Andrade, R. E., Vondenhoff, K., Keller, J., Delaux, P.-M., Hayashi, M.,
893 Griesmann, M., & Parniske, M. (2022). A novel cis-element enabled bacterial uptake by plant
894 cells (p. 2022.03.28.486070). *bioRxiv*. https://doi.org/10.1101/2022.03.28.486070
895 Cebolla, A., Vinardell, J. M., Kiss, E., Olah, B., Roudier, F., Kondorosi, A., & Kondorosi, E. (1999).
896 The mitotic inhibitor ccs52 is required for endoreduplication and ploidy-dependent cell
897 enlargement in plants. *EMBO J*, *18*(16), 4476-4484.
898 https://doi.org/10.1093/emboj/18.16.4476
899 Chen, P., Takatsuka, H., Takahashi, N., Kurata, R., Fukao, Y., Kobayashi, K., Ito, M., & Umeda, M.
900 (2017). Arabidopsis R1R2R3-Myb proteins are essential for inhibiting cell division in
901 response to DNA damage. *Nat Commun*, *8*(1), Article 1. https://doi.org/10.1038/s41467-017-
902 00676-4
903 Colón-Carmona, A., You, R., Haimovitch-Gal, T., & Doerner, P. (1999). Technical advance : Spatio-
904 temporal analysis of mitotic activity with a labile cyclin-GUS fusion protein. *Plant J*, *20*(4),
905 503-508. https://doi.org/10.1046/j.1365-313x.1999.00620.x
906 Combier, J. P., Frugier, F., de Billy, F., Boualem, A., El-Yahyaoui, F., Moreau, S., Vernie, T., Ott,
907 T., Gamas, P., Crespi, M., & Niebel, A. (2006). MtHAP2-1 is a key transcriptional regulator
908 of symbiotic nodule development regulated by microRNA169 in Medicago truncatula. *Genes*
909 *Dev*, *20*(22), 3084-3088. https://doi.org/10.1101/gad.402806
910 Cosolo, A., Jaiswal, J., Csordas, G., Grass, I., Uhlirova, M., & Classen, A. K. (2019). JNK-dependent
911 cell cycle stalling in G2 promotes survival and senescence-like phenotypes in tissue stress.
912 *Elife*, *8*. https://doi.org/10.7554/eLife.41036
913 Costa, S. (2017). Are division plane determination and cell-cycle progression coordinated? *New*
914 *Phytol*, *213*(1), 16-21. https://doi.org/10.1111/nph.14261
915 Davarinejad, H., Huang, Y. C., Mermaz, B., LeBlanc, C., Poulet, A., Thomson, G., Joly, V., Munoz,
916 M., Arvanitis-Vigneault, A., Valsakumar, D., Villarino, G., Ross, A., Rotstein, B. H., Alarcon,

917 E. I., Brunzelle, J. S., Voigt, P., Dong, J., Couture, J. F., & Jacob, Y. (2022). The histone H3.1
918 variant regulates TONSOKU-mediated DNA repair during replication. *Science*, *375*(6586),
919 1281-1286. https://doi.org/10.1126/science.abm5320
920 De Storme, N., Keceli, B. N., Zamariola, L., Angenon, G., & Geelen, D. (2016). CENH3-GFP: a
921 visual marker for gametophytic and somatic ploidy determination in Arabidopsis thaliana.
922 *BMC Plant Biol*, *16*, 1. https://doi.org/10.1186/s12870-015-0700-5
923 De Veylder, L., Larkin, J. C., & Schnittger, A. (2011). Molecular control and function of
924 endoreplication in development and physiology. *Trends Plant Sci*, *16*(11), 624-634.
925 https://doi.org/10.1016/j.tplants.2011.07.001
926 Desvoyes, B., Arana-Echarri, A., Barea, M. D., & Gutierrez, C. (2020). A comprehensive fluorescent
927 sensor for spatiotemporal cell cycle analysis in Arabidopsis. *Nat Plants*, *6*(11), 1330-1334.
928 https://doi.org/10.1038/s41477-020-00770-4
929 Desvoyes, B., Noir, S., Masoud, K., López, M. I., Genschik, P., & Gutierrez, C. (2019). FBL17 targets
930 CDT1a for degradation in early S-phase to prevent Arabidopsis genome instability (p.
931 774109). *bioRxiv*. https://doi.org/10.1101/774109
932 Dewitte, W., Riou-Khamlichi, C., Scofield, S., Healy, J. M. S., Jacqmard, A., Kilby, N. J., & Murray,
933 J. A. H. (2003). Altered Cell Cycle Distribution, Hyperplasia, and Inhibited Differentiation in
934 Arabidopsis Caused by the D-Type Cyclin CYCD3. *Plant Cell*, *15*(1), 79-92.
935 https://doi.org/10.1105/tpc.004838
936 Di Agostino, S., Strano, S., Emiliozzi, V., Zerbini, V., Mottolese, M., Sacchi, A., Blandino, G., &
937 Piaggio, G. (2006). Gain of function of mutant p53 : The mutant p53/NF-Y protein complex
938 reveals an aberrant transcriptional mechanism of cell cycle regulation. *Cancer Cell*, *10*(3),
939 191-202. https://doi.org/10.1016/j.ccr.2006.08.013
940 Dong, W., Zhu, Y., Chang, H., Wang, C., Yang, J., Shi, J., Gao, J., Yang, W., Lan, L., Wang, Y.,
941 Zhang, X., Dai, H., Miao, Y., Xu, L., He, Z., Song, C., Wu, S., Wang, D., Yu, N., & Wang,
942 E. (2021). An SHR-SCR module specifies legume cortical cell fate to enable nodulation.
943 *Nature*, *589*(7843), 586-590. https://doi.org/10.1038/s41586-020-3016-z
944 Doyle, J. J., & Coate, J. E. (2019). Polyploidy, the Nucleotype, and Novelty : The Impact of Genome
945 Doubling on the Biology of the Cell. *Int J Plant Sci*, *180*(1), 1-52.
946 https://doi.org/10.1086/700636
947 Draizen, E. J., Shaytan, A. K., Marino-Ramirez, L., Talbert, P. B., Landsman, D., & Panchenko, A.
948 R. (2016). HistoneDB 2.0 : A histone database with variants—An integrated resource to
949 explore histones and their variants. *Database (Oxford)*, *2016*.
950 https://doi.org/10.1093/database/baw014

Echevarría, C., Gutierrez, C., & Desvoyes, B. (2021). Tools for Assessing Cell-Cycle Progression in Plants. *Plant and Cell Physiology*, *62*(8), 1231-1238. https://doi.org/10.1093/pcp/pcab066

Edgar, B. A., Zielke, N., & Gutierrez, C. (2014). Endocycles : A recurrent evolutionary innovation for post-mitotic cell growth. *Nat Rev Mol Cell Biol*, *15*(3), 197-210. https://doi.org/10.1038/nrm3756

Feng, J., Lee, T., Schiessl, K., & Oldroyd, G. E. D. (2021). Processing of NODULE INCEPTION controls the transition to nitrogen fixation in root nodules. *Science*, *374*(6567), 629-632. https://doi.org/10.1126/science.abg2804

Foucher, F., & Kondorosi, E. (2000). Cell cycle regulation in the course of nodule organogenesis in Medicago. *Plant Mol Biol*, *43*(5-6), 773-786. https://doi.org/10.1023/a:1006405029600

Fournier, J., Teillet, A., Chabaud, M., Ivanov, S., Genre, A., Limpens, E., de Carvalho-Niebel, F., & Barker, D. G. (2015). Remodeling of the infection chamber before infection thread formation reveals a two-step mechanism for rhizobial entry into the host legume root hair. *Plant Physiol*, *167*(4), 1233-1242. https://doi.org/10.1104/pp.114.253302

Fulop, K., Tarayre, S., Kelemen, Z., Horvath, G., Kevei, Z., Nikovics, K., Bako, L., Brown, S., Kondorosi, A., & Kondorosi, E. (2005). Arabidopsis anaphase-promoting complexes : Multiple activators and wide range of substrates might keep APC perpetually busy. *Cell Cycle*, *4*(8), 1084-1092.

Gao, J. P., Jiang, S., Su, Y., Xu, P., Wang, J., Liang, W., Liu, C. W., & Murray, J. D. (2022). Intracellular infection by symbiotic bacteria requires the mitotic kinase AURORA1. *Proc Natl Acad Sci U S A*, *119*(43), e2202606119. https://doi.org/10.1073/pnas.2202606119

Gaudioso-Pedraza, R., Beck, M., Frances, L., Kirk, P., Ripodas, C., Niebel, A., Oldroyd, G. E. D., Benitez-Alfonso, Y., & de Carvalho-Niebel, F. (2018). Callose-Regulated Symplastic Communication Coordinates Symbiotic Root Nodule Development. *Curr Biol*, *28*(22), 3562-3577 e6. https://doi.org/10.1016/j.cub.2018.09.031

Gauthier-Coles, C., White, R. G., & Mathesius, U. (2018). Nodulating Legumes Are Distinguished by a Sensitivity to Cytokinin in the Root Cortex Leading to Pseudonodule Development. *Front Plant Sci*, *9*, 1901. https://doi.org/10.3389/fpls.2018.01901

Gigli-Bisceglia, N., Engelsdorf, T., Strnad, M., Vaahtera, L., Khan, G. A., Yamoune, A., Alipanah, L., Novak, O., Persson, S., Hejatko, J., & Hamann, T. (2018). Cell wall integrity modulates Arabidopsis thaliana cell cycle gene expression in a cytokinin- and nitrate reductase-dependent manner. *Development*, *145*(19). https://doi.org/10.1242/dev.166678

983 Gleason, C., Chaudhuri, S., Yang, T., Munoz, A., Poovaiah, B. W., & Oldroyd, G. E. (2006).
984 Nodulation independent of rhizobia induced by a calcium-activated kinase lacking
985 autoinhibition. *Nature*, *441*(7097), 1149-1152. https://doi.org/10.1038/nature04812
986 Goodstein, D. M., Shu, S., Howson, R., Neupane, R., Hayes, R. D., Fazo, J., Mitros, T., Dirks, W.,
987 Hellsten, U., Putnam, N., & Rokhsar, D. S. (2012). Phytozome : A comparative platform for
988 green plant genomics. *Nucleic Acids Res*, *40*(Database issue), D1178-86.
989 https://doi.org/10.1093/nar/gkr944
990 Guan, D., Stacey, N., Liu, C., Wen, J., Mysore, K. S., Torres-Jerez, I., Vernié, T., Tadege, M., Zhou,
991 C., Wang, Z., Udvardi, M. K., Oldroyd, G. E. D., & Murray, J. D. (2013). Rhizobial Infection
992 Is Associated with the Development of Peripheral Vasculature in Nodules of Medicago
993 truncatula1[W][OA]. *Plant Physiol*, *162*(1), 107-115. https://doi.org/10.1104/pp.113.215111
994 Haga, N., Kato, K., Murase, M., Araki, S., Kubo, M., Demura, T., Suzuki, K., Muller, I., Voss, U.,
995 Jurgens, G., & Ito, M. (2007). R1R2R3-Myb proteins positively regulate cytokinesis through
996 activation of KNOLLE transcription in Arabidopsis thaliana. *Development*, *134*(6),
997 1101-1110. https://doi.org/10.1242/dev.02801
998 Hayashi, T., Banba, M., Shimoda, Y., Kouchi, H., Hayashi, M., & Imaizumi-Anraku, H. (2010). A
999 dominant function of CCaMK in intracellular accommodation of bacterial and fungal
1000 endosymbionts. *Plant J*, *63*(1), 141-154. https://doi.org/10.1111/j.1365-313X.2010.04228.x
1001 Hernandez-Lagana, E., & Autran, D. (2020). H3.1 Eviction Marks Female Germline Precursors in
1002 Arabidopsis. *Plants*, *9*(10), Article 10. https://doi.org/10.3390/plants9101322
1003 Hernandez-Lagana, E., Mosca, G., Mendocilla-Sato, E., Pires, N., Frey, A., Giraldo-Fonseca, A.,
1004 Michaud, C., Grossniklaus, U., Hamant, O., Godin, C., Boudaoud, A., Grimanelli, D., Autran,
1005 D., & Baroux, C. (2021). Organ geometry channels reproductive cell fate in the Arabidopsis
1006 ovule primordium. *Elife*, *10*. https://doi.org/10.7554/eLife.66031
1007 Hirsch, C. D., Wu, Y., Yan, H., & Jiang, J. (2009). Lineage-specific adaptive evolution of the
1008 centromeric protein CENH3 in diploid and allotetraploid Oryza species. *Mol Biol Evol*,
1009 *26*(12), 2877-2885. https://doi.org/10.1093/molbev/msp208
1010 Hossain, M. S., Shrestha, A., Zhong, S., Miri, M., Austin, R. S., Sato, S., Ross, L., Huebert, T.,
1011 Tromas, A., Torres-Jerez, I., Tang, Y., Udvardi, M., Murray, J. D., & Szczyglowski, K.
1012 (2016). Lotus japonicus NF-YA1 Plays an Essential Role During Nodule Differentiation and
1013 Targets Members of the SHI/STY Gene Family. *Mol Plant Microbe Interact*, *29*(12), 950-964.
1014 https://doi.org/10.1094/MPMI-10-16-0206-R
1015 Imbriano, C., Gurtner, A., Cocchiarella, F., Di Agostino, S., Basile, V., Gostissa, M., Dobbelstein,
1016 M., Del Sal, G., Piaggio, G., & Mantovani, R. (2005). Direct p53 transcriptional repression :

1017 In vivo analysis of CCAAT-containing G2/M promoters. *Mol Cell Biol*, *25*(9), 3737-3751.
1018 https://doi.org/10.1128/MCB.25.9.3737-3751.2005
1019 Ingouff, M., Rademacher, S., Holec, S., Soljic, L., Xin, N., Readshaw, A., Foo, S. H., Lahouze, B.,
1020 Sprunck, S., & Berger, F. (2010). Zygotic resetting of the HISTONE 3 variant repertoire
1021 participates in epigenetic reprogramming in Arabidopsis. *Curr Biol*, *20*(23), 2137-2143.
1022 https://doi.org/10.1016/j.cub.2010.11.012
1023 Ito, M., Araki, S., Matsunaga, S., Itoh, T., Nishihama, R., Machida, Y., Doonan, J. H., & Watanabe,
1024 A. (2001). G2/M-phase-specific transcription during the plant cell cycle is mediated by c-
1025 Myb-like transcription factors. *Plant Cell*, *13*(8), 1891-1905.
1026 https://doi.org/10.1105/tpc.010102
1027 Iwata, E., Ikeda, S., Matsunaga, S., Kurata, M., Yoshioka, Y., Criqui, M. C., Genschik, P., & Ito, M.
1028 (2011). GIGAS CELL1, a novel negative regulator of the anaphase-promoting
1029 complex/cyclosome, is required for proper mitotic progression and cell fate determination in
1030 Arabidopsis. *Plant Cell*, *23*(12), 4382-4393. https://doi.org/10.1105/tpc.111.092049
1031 Jiang, D., & Berger, F. (2017). DNA replication–coupled histone modification maintains Polycomb
1032 gene silencing in plants. *Science*, *357*(6356), 1146-1149.
1033 https://doi.org/10.1126/science.aan4965
1034 Karimi-Ashtiyani, R., Ishii, T., Niessen, M., Stein, N., Heckmann, S., Gurushidze, M., Banaei-
1035 Moghaddam, A. M., Fuchs, J., Schubert, V., Koch, K., Weiss, O., Demidov, D., Schmidt, K.,
1036 Kumlehn, J., & Houben, A. (2015). Point mutation impairs centromeric CENH3 loading and
1037 induces haploid plants. *Proc Natl Acad Sci U S A*, *112*(36), 11211-11216.
1038 https://doi.org/10.1073/pnas.1504333112
1039 Knaack, S. A., Conde, D., Chakraborty, S., Balmant, K. M., Irving, T. B., Maia, L. G. S., Triozzi, P.
1040 M., Dervinis, C., Pereira, W. J., Maeda, J., Schmidt, H. W., Ane, J. M., Kirst, M., & Roy, S.
1041 (2022). Temporal change in chromatin accessibility predicts regulators of nodulation in
1042 Medicago truncatula. *BMC Biol*, *20*(1), 252. https://doi.org/10.1186/s12915-022-01450-9
1043 Kobayashi, K., Suzuki, T., Iwata, E., Nakamichi, N., Suzuki, T., Chen, P., Ohtani, M., Ishida, T.,
1044 Hosoya, H., Müller, S., Leviczky, T., Pettkó-Szandtner, A., Darula, Z., Iwamoto, A., Nomoto,
1045 M., Tada, Y., Higashiyama, T., Demura, T., Doonan, J. H., … Ito, M. (2015). Transcriptional
1046 repression by MYB3R proteins regulates plant organ growth. *The EMBO Journal*, *34*(15),
1047 1992-2007. https://doi.org/10.15252/embj.201490899
1048 Kondorosi, E., & Kondorosi, A. (2004). Endoreduplication and activation of the anaphase-promoting
1049 complex during symbiotic cell development. *FEBS Lett*, *567*(1), 152-157.
1050 https://doi.org/10.1016/j.febslet.2004.04.075

1051 Lace, B., Su, C., Invernot Perez, D., Rodriguez-Franco, M., Vernie, T., Batzenschlager, M., Egli, S.,
1052 Liu, C. W., & Ott, T. (2023). RPG acts as a central determinant for infectosome formation
1053 and cellular polarization during intracellular rhizobial infections. *Elife*, *12*.
1054 https://doi.org/10.7554/eLife.80741
1055 Laloum, T., Baudin, M., Frances, L., Lepage, A., Billault-Penneteau, B., Cerri, M. R., Ariel, F.,
1056 Jardinaud, M.-F., Gamas, P., de Carvalho-Niebel, F., & Niebel, A. (2014). Two CCAAT-box-
1057 binding transcription factors redundantly regulate early steps of the legume-rhizobia
1058 endosymbiosis. *Plant J*, *79*(5), 757-768. https://doi.org/10.1111/tpj.12587
1059 Laporte, P., Lepage, A., Fournier, J., Catrice, O., Moreau, S., Jardinaud, M. F., Mun, J. H., Larrainzar,
1060 E., Cook, D. R., Gamas, P., & Niebel, A. (2014). The CCAAT box-binding transcription
1061 factor NF-YA1 controls rhizobial infection. *J Exp Bot*, *65*(2), 481-494.
1062 https://doi.org/10.1093/jxb/ert392
1063 Lermontova, I., Rutten, T., & Schubert, I. (2011). Deposition, turnover, and release of CENH3 at
1064 Arabidopsis centromeres. *Chromosoma*, *120*(6), 633-640. https://doi.org/10.1007/s00412-
1065 011-0338-5
1066 Lermontova, I., Schubert, V., Bornke, F., Macas, J., & Schubert, I. (2007). Arabidopsis CBF5
1067 interacts with the H/ACA snoRNP assembly factor NAF1. *Plant Mol Biol*, *65*(5), 615-626.
1068 https://doi.org/10.1007/s11103-007-9226-z
1069 Lermontova, I., Schubert, V., Fuchs, J., Klatte, S., Macas, J., & Schubert, I. (2006). Loading of
1070 Arabidopsis centromeric histone CENH3 occurs mainly during G2 and requires the presence
1071 of the histone fold domain. *Plant Cell*, *18*(10), 2443-2451.
1072 https://doi.org/10.1105/tpc.106.043174
1073 Liang, J., Klingl, A., Lin, Y.-Y., Boul, E., Thomas-Oates, J., & Marín, M. (2019). A subcompatible
1074 rhizobium strain reveals infection duality in Lotus. *J Exp Bot*, *70*(6), 1903-1913.
1075 https://doi.org/10.1093/jxb/erz057
1076 Libbenga, K. R., & Torrey, J. G. (1973). Hormone-Induced Endoreduplication Prior to Mitosis in
1077 Cultured Pea Root Cortex Cells. *Am J Bot*, *60*(4), 293-299. https://doi.org/10.2307/2441195
1078 Linhart, C., Elkon, R., Shiloh, Y., & Shamir, R. (2005). Deciphering transcriptional regulatory
1079 elements that encode specific cell cycle phasing by comparative genomics analysis. *Cell*
1080 *Cycle*, *4*(12), 1788-1797. https://doi.org/10.4161/cc.4.12.2173
1081 Liu, C. W., Breakspear, A., Stacey, N., Findlay, K., Nakashima, J., Ramakrishnan, K., Liu, M., Xie,
1082 F., Endre, G., de Carvalho-Niebel, F., Oldroyd, G. E. D., Udvardi, M. K., Fournier, J., &
1083 Murray, J. D. (2019a). A protein complex required for polar growth of rhizobial infection
1084 threads. *Nat Commun*, *10*(1), 2848. https://doi.org/10.1038/s41467-019-10029-y

1085 Liu, H., Lin, J.-S., Luo, Z., Sun, J., Huang, X., Yang, Y., Xu, J., Wang, Y.-F., Zhang, P., Oldroyd, G.
1086 E. D., & Xie, F. (2022). Constitutive activation of a nuclear-localized calcium channel
1087 complex in Medicago truncatula. *Proc Natl Acad Sci U S A*, *119*(34), e2205920119.
1088 https://doi.org/10.1073/pnas.2205920119
1089 Liu, J., Rutten, L., Limpens, E., van der Molen, T., van Velzen, R., Chen, R., Chen, Y., Geurts, R.,
1090 Kohlen, W., Kulikova, O., & Bisseling, T. (2019b). A Remote cis-Regulatory Region Is
1091 Required for NIN Expression in the Pericycle to Initiate Nodule Primordium Formation in
1092 Medicago truncatula. *Plant Cell*, *31*(1), 68-83. https://doi.org/10.1105/tpc.18.00478
1093 Lu, L., Chen, X., Qian, S., & Zhong, X. (2018). The plant-specific histone residue Phe41 is important
1094 for genome-wide H3.1 distribution. *Nat Commun*, *9*(1), Article 1.
1095 https://doi.org/10.1038/s41467-018-02976-9
1096 Ma, Y., Jonsson, K., Aryal, B., De Veylder, L., Hamant, O., & Bhalerao, R. P. (2022).
1097 Endoreplication mediates cell size control via mechanochemical signaling from cell wall. *Sci*
1098 *Adv*, *8*(49), eabq2047. https://doi.org/10.1126/sciadv.abq2047
1099 Madsen, L. H., Tirichine, L., Jurkiewicz, A., Sullivan, J. T., Heckmann, A. B., Bek, A. S., Ronson,
1100 C. W., James, E. K., & Stougaard, J. (2010). The molecular network governing nodule
1101 organogenesis and infection in the model legume Lotus japonicus. *Nat Commun*, *1*(1), 10.
1102 https://doi.org/10.1038/ncomms1009
1103 Manni, I., Mazzaro, G., Gurtner, A., Mantovani, R., Haugwitz, U., Krause, K., Engeland, K., Sacchi,
1104 A., Soddu, S., & Piaggio, G. (2001). NF-Y mediates the transcriptional inhibition of the cyclin
1105 B1, cyclin B2, and cdc25C promoters upon induced G2 arrest. *J Biol Chem*, *276*(8),
1106 5570-5576. https://doi.org/10.1074/jbc.M006052200
1107 Marsh, J. F., Rakocevic, A., Mitra, R. M., Brocard, L., Sun, J., Eschstruth, A., Long, S. R., Schultze,
1108 M., Ratet, P., & Oldroyd, G. E. (2007). Medicago truncatula NIN is essential for rhizobial-
1109 independent nodule organogenesis induced by autoactive calcium/calmodulin-dependent
1110 protein kinase. *Plant Physiol*, *144*(1), 324-335. https://doi.org/10.1104/pp.106.093021
1111 McCloy, R. A., Rogers, S., Caldon, C. E., Lorca, T., Castro, A., & Burgess, A. (2014). Partial
1112 inhibition of Cdk1 in G 2 phase overrides the SAC and decouples mitotic events. *Cell Cycle*,
1113 *13*(9), 1400-1412. https://doi.org/10.4161/cc.28401
1114 Meserve, J. H., & Duronio, R. J. (2017). A population of G2-arrested cells are selected as sensory
1115 organ precursors for the interommatidial bristles of the Drosophila eye. *Dev Biol*, *430*(2),
1116 374-384. https://doi.org/10.1016/j.ydbio.2017.06.023
1117 Meyer, H. M., Teles, J., Formosa-Jordan, P., Refahi, Y., San-Bento, R., Ingram, G., Jönsson, H.,
1118 Locke, J. C. W., & Roeder, A. H. K. (2017). Fluctuations of the transcription factor ATML1

1119 generate the pattern of giant cells in the Arabidopsis sepal. *eLife*, *6*, e19131.
1120 https://doi.org/10.7554/eLife.19131
1121 Monroy-Morales, E., Davila-Delgado, R., Ayala-Guzman, E., Gamboa-deBuen, A., & Sanchez-
1122 Lopez, R. (2022). Visualization of the Crossroads between a Nascent Infection Thread and
1123 the First Cell Division Event in Phaseolus vulgaris Nodulation. *Int J Mol Sci*, *23*(9).
1124 https://doi.org/10.3390/ijms23095267
1125 Mutterer, J., & Zinck, E. (2013). Quick-and-clean article figures with FigureJ. *J Microsc*, *252*(1),
1126 89-91. https://doi.org/10.1111/jmi.12069
1127 Myers, Z. A., & Holt, B. F. (2018). NUCLEAR FACTOR-Y: still complex after all these years? *Curr*
1128 *Opin Plant Biol*, *45*(Pt A), 96-102. https://doi.org/10.1016/j.pbi.2018.05.015
1129 Nadzieja, M., Stougaard, J., & Reid, D. (2019). A Toolkit for High Resolution Imaging of Cell
1130 Division and Phytohormone Signaling in Legume Roots and Root Nodules. *Front Plant Sci*,
1131 *10*, 1000. https://doi.org/10.3389/fpls.2019.01000
1132 Nagymihaly, M., Veluchamy, A., Gyorgypal, Z., Ariel, F., Jegu, T., Benhamed, M., Szucs, A.,
1133 Kereszt, A., Mergaert, P., & Kondorosi, E. (2017). Ploidy-dependent changes in the
1134 epigenome of symbiotic cells correlate with specific patterns of gene expression. *Proc Natl*
1135 *Acad Sci U S A*, *114*(17), 4543-4548. https://doi.org/10.1073/pnas.1704211114
1136 Negishi, T., Veis, J., Hollenstein, D., Sekiya, M., Ammerer, G., & Ohya, Y. (2016). The Late S-Phase
1137 Transcription Factor Hcm1 Is Regulated through Phosphorylation by the Cell Wall Integrity
1138 Checkpoint. *Mol Cell Biol*, *36*(6), 941-953. https://doi.org/10.1128/MCB.00952-15
1139 Otero, S., Desvoyes, B., Peiro, R., & Gutierrez, C. (2016). Histone H3 Dynamics Reveal Domains
1140 with Distinct Proliferation Potential in the Arabidopsis Root. *Plant Cell*, *28*(6), 1361-1371.
1141 https://doi.org/10.1105/tpc.15.01003
1142 Park, M., Krause, C., Karnahl, M., Reichardt, I., El Kasmi, F., Mayer, U., Stierhof, Y. D., Hiller, U.,
1143 Strompen, G., Bayer, M., Kientz, M., Sato, M. H., Nishimura, M. T., Dangl, J. L., Sanderfoot,
1144 A. A., & Jurgens, G. (2018). Concerted Action of Evolutionarily Ancient and Novel SNARE
1145 Complexes in Flowering-Plant Cytokinesis. *Dev Cell*, *44*(4), 500-511 e4.
1146 https://doi.org/10.1016/j.devcel.2017.12.027
1147 Parniske, M. (2018). Uptake of bacteria into living plant cells, the unifying and distinct feature of the
1148 nitrogen-fixing root nodule symbiosis. *Curr Opin Plant Biol*, *44*, 164-174.
1149 https://doi.org/10.1016/j.pbi.2018.05.016
1150 Pecrix, Y., Staton, S. E., Sallet, E., Lelandais-Briere, C., Moreau, S., Carrere, S., Blein, T., Jardinaud,
1151 M. F., Latrasse, D., Zouine, M., Zahm, M., Kreplak, J., Mayjonade, B., Satge, C., Perez, M.,
1152 Cauet, S., Marande, W., Chantry-Darmon, C., Lopez-Roques, C., … Gamas, P. (2018).

1153 Whole-genome landscape of Medicago truncatula symbiotic genes. *Nat Plants*, *4*(12),
1154 1017-1025. https://doi.org/10.1038/s41477-018-0286-7
1155 Probst, A. V., Desvoyes, B., & Gutierrez, C. (2020). Similar yet critically different : The distribution,
1156 dynamics and function of histone variants. *J Exp Bot*, *71*(17), 5191-5204.
1157 https://doi.org/10.1093/jxb/eraa230
1158 Procter, J. B., Carstairs, G. M., Soares, B., Mourao, K., Ofoegbu, T. C., Barton, D., Lui, L., Menard,
1159 A., Sherstnev, N., Roldan-Martinez, D., Duce, S., Martin, D. M. A., & Barton, G. J. (2021).
1160 Alignment of Biological Sequences with Jalview. *Methods Mol Biol*, *2231*, 203-224.
1161 https://doi.org/10.1007/978-1-0716-1036-7_13
1162 Ried, M. K., Antolin-Llovera, M., & Parniske, M. (2014). Spontaneous symbiotic reprogramming of
1163 plant roots triggered by receptor-like kinases. *Elife*, *3*. https://doi.org/10.7554/eLife.03891
1164 Rivera, H. E., & Davies, S. W. (2021). Symbiosis maintenance in the facultative coral, Oculina
1165 arbuscula, relies on nitrogen cycling, cell cycle modulation, and immunity. *Sci Rep*, *11*(1),
1166 21226. https://doi.org/10.1038/s41598-021-00697-6
1167 Rost, T. L. (2011). The organization of roots of dicotyledonous plants and the positions of control
1168 points. *Ann Bot*, *107*(7), 1213-1222. https://doi.org/10.1093/aob/mcq229
1169 Roux, B., Rodde, N., Jardinaud, M. F., Timmers, T., Sauviac, L., Cottret, L., Carrere, S., Sallet, E.,
1170 Courcelle, E., Moreau, S., Debelle, F., Capela, D., de Carvalho-Niebel, F., Gouzy, J., Bruand,
1171 C., & Gamas, P. (2014). An integrated analysis of plant and bacterial gene expression in
1172 symbiotic root nodules using laser-capture microdissection coupled to RNA sequencing.
1173 *Plant J*, *77*(6), 817-837. https://doi.org/10.1111/tpj.12442
1174 Russo, G., Carotenuto, G., Fiorilli, V., Volpe, V., Chiapello, M., Van Damme, D., & Genre, A.
1175 (2019). Ectopic activation of cortical cell division during the accommodation of arbuscular
1176 mycorrhizal fungi. *New Phytol*, *221*(2), 1036-1048. https://doi.org/10.1111/nph.15398
1177 Russo, G., & Genre, A. (2021). Divide and Be Conquered-Cell Cycle Reactivation in Arbuscular
1178 Mycorrhizal Symbiosis. *Front Plant Sci*, *12*, 753265.
1179 https://doi.org/10.3389/fpls.2021.753265
1180 Sanei, M., Pickering, R., Kumke, K., Nasuda, S., & Houben, A. (2011). Loss of centromeric histone
1181 H3 (CENH3) from centromeres precedes uniparental chromosome elimination in interspecific
1182 barley hybrids. *Proc Natl Acad Sci U S A*, *108*(33), E498-505.
1183 https://doi.org/10.1073/pnas.1103190108
1184 Schaefer, E., Belcram, K., Uyttewaal, M., Duroc, Y., Goussot, M., Legland, D., Laruelle, E.,
1185 de Tauzia-Moreau, M. L., Pastuglia, M., & Bouchez, D. (2017). The preprophase band of

microtubules controls the robustness of division orientation in plants. *Science*, *356*(6334), 186-189. https://doi.org/10.1126/science.aal3016

Schauser, L., Roussis, A., Stiller, J., & Stougaard, J. (1999). A plant regulator controlling development of symbiotic root nodules. *Nature*, *402*(6758), 191-195. https://doi.org/10.1038/46058

Schiessl, K., Lee, T., Orvosova, M., Bueno-Batista, M., Stuer, N., Bailey, P. C., Mysore, K. S., Wen, J., & Oldroyd, G. E. D. (2023). *Light sensitive short hypocotyl (LSH) confer symbiotic nodule identity in the legume Medicago truncatula* (p. 2023.02.12.528179). bioRxiv. https://doi.org/10.1101/2023.02.12.528179

Schiessl, K., Lilley, J. L. S., Lee, T., Tamvakis, I., Kohlen, W., Bailey, P. C., Thomas, A., Luptak, J., Ramakrishnan, K., Carpenter, M. D., Mysore, K. S., Wen, J., Ahnert, S., Grieneisen, V. A., & Oldroyd, G. E. D. (2019). NODULE INCEPTION Recruits the Lateral Root Developmental Program for Symbiotic Nodule Organogenesis in Medicago truncatula. *Curr Biol*, *29*(21), 3657-3668 e5. https://doi.org/10.1016/j.cub.2019.09.005

Schindelin, J., Arganda-Carreras, I., Frise, E., Kaynig, V., Longair, M., Pietzsch, T., Preibisch, S., Rueden, C., Saalfeld, S., Schmid, B., Tinevez, J. Y., White, D. J., Hartenstein, V., Eliceiri, K., Tomancak, P., & Cardona, A. (2012). Fiji : An open-source platform for biological-image analysis. *Nat Methods*, *9*(7), 676-682. https://doi.org/10.1038/nmeth.2019

Schnittger, A., Schöbinger, U., Bouyer, D., Weinl, C., Stierhof, Y.-D., & Hülskamp, M. (2002). Ectopic D-type cyclin expression induces not only DNA replication but also cell division in Arabidopsis trichomes. *Proc Natl Acad Sci U S A*, *99*(9), 6410-6415. https://doi.org/10.1073/pnas.092657299

Shi, L., Wang, J., Hong, F., Spector, D. L., & Fang, Y. (2011). Four amino acids guide the assembly or disassembly of Arabidopsis histone H3.3-containing nucleosomes. *Proc Natl Acad Sci U S A*, *108*(26), 10574-10578. https://doi.org/10.1073/pnas.1017882108

Shimotohno, A., Aki, S. S., Takahashi, N., & Umeda, M. (2021). Regulation of the Plant Cell Cycle in Response to Hormones and the Environment. *Annu Rev Plant Biol*, *72*, 273-296. https://doi.org/10.1146/annurev-arplant-080720-103739

Shrestha, A., Zhong, S., Therrien, J., Huebert, T., Sato, S., Mun, T., Andersen, S. U., Stougaard, J., Lepage, A., Niebel, A., Ross, L., & Szczyglowski, K. (2021). Lotus japonicus Nuclear Factor YA1, a nodule emergence stage-specific regulator of auxin signalling. *New Phytol*, *229*(3), 1535-1552. https://doi.org/10.1111/nph.16950

1218 Silhavy, D., Molnar, A., Lucioli, A., Szittya, G., Hornyik, C., Tavazza, M., & Burgyan, J. (2002). A
1219 viral protein suppresses RNA silencing and binds silencing-generated, 21- to 25-nucleotide
1220 double-stranded RNAs. *EMBO J*, *21*(12), 3070-3080. https://doi.org/10.1093/emboj/cdf312
1221 Singh, S., Katzer, K., Lambert, J., Cerri, M., & Parniske, M. (2014). CYCLOPS, a DNA-binding
1222 transcriptional activator, orchestrates symbiotic root nodule development. *Cell Host Microbe*,
1223 *15*(2), 139-152. https://doi.org/10.1016/j.chom.2014.01.011
1224 Smertenko, A., Assaad, F., Baluška, F., Bezanilla, M., Buschmann, H., Drakakaki, G., Hauser, M.-
1225 T., Janson, M., Mineyuki, Y., Moore, I., Müller, S., Murata, T., Otegui, M. S., Panteris, E.,
1226 Rasmussen, C., Schmit, A.-C., Šamaj, J., Samuels, L., Staehelin, L. A., … Žárský, V. (2017).
1227 Plant Cytokinesis : Terminology for Structures and Processes. *Trends Cell Biol*, *27*(12),
1228 885-894. https://doi.org/10.1016/j.tcb.2017.08.008
1229 Soni, R., Carmichael, J. P., Shah, Z. H., & Murray, J. A. (1995). A family of cyclin D homologs from
1230 plants differentially controlled by growth regulators and containing the conserved
1231 retinoblastoma protein interaction motif. *Plant Cell*, *7*(1), 85-103.
1232 https://doi.org/10.1105/tpc.7.1.85
1233 Soyano, T., Hirakawa, H., Sato, S., Hayashi, M., & Kawaguchi, M. (2014). Nodule Inception creates
1234 a long-distance negative feedback loop involved in homeostatic regulation of nodule organ
1235 production. *Proc Natl Acad Sci U S A*, *111*(40), 14607-14612.
1236 https://doi.org/10.1073/pnas.1412716111
1237 Soyano, T., Kouchi, H., Hirota, A., & Hayashi, M. (2013). Nodule inception directly targets NF-Y
1238 subunit genes to regulate essential processes of root nodule development in Lotus japonicus.
1239 *PLoS Genet*, *9*(3), e1003352. https://doi.org/10.1371/journal.pgen.1003352
1240 Su, C., Zhang, G., Rodriguez-Franco, M., Hinnenberg, R., Wietschorke, J., Liang, P., Yang, W.,
1241 Uhler, L., Li, X., & Ott, T. (2023). Transcellular progression of infection threads in Medicago
1242 truncatula roots is associated with locally confined cell wall modifications. *Curr Biol*, *33*(3),
1243 533-542 e5. https://doi.org/10.1016/j.cub.2022.12.051
1244 Suzaki, T., Ito, M., Yoro, E., Sato, S., Hirakawa, H., Takeda, N., & Kawaguchi, M. (2014).
1245 Endoreduplication-mediated initiation of symbiotic organ development in Lotus japonicus.
1246 *Development*, *141*(12), 2441-2445. https://doi.org/10.1242/dev.107946
1247 Takahashi, N., Ogita, N., Takahashi, T., Taniguchi, S., Tanaka, M., Seki, M., & Umeda, M. (2019).
1248 A regulatory module controlling stress-induced cell cycle arrest in Arabidopsis. *Elife*, *8*.
1249 https://doi.org/10.7554/eLife.43944

1250 Talbert, P. B., Masuelli, R., Tyagi, A. P., Comai, L., & Henikoff, S. (2002). Centromeric localization
1251 and adaptive evolution of an Arabidopsis histone H3 variant. *Plant Cell*, *14*(5), 1053-1066.
1252 https://doi.org/10.1105/tpc.010425
1253 Tek, A. L., Kashihara, K., Murata, M., & Nagaki, K. (2014). Identification of the centromere-specific
1254 histone H3 variant in Lotus japonicus. *Gene*, *538*(1), 8-11.
1255 https://doi.org/10.1016/j.gene.2014.01.034
1256 Timmers, A. C., Auriac, M. C., & Truchet, G. (1999). Refined analysis of early symbiotic steps of
1257 the Rhizobium-Medicago interaction in relationship with microtubular cytoskeleton
1258 rearrangements. *Development*, *126*(16), 3617-3628. https://doi.org/10.1242/dev.126.16.3617
1259 Torrey, J. G., & Barrios, S. (1969). Cytological Studies on Rhizobial Nodule Initiation in Pisum.
1260 *Caryologia*, *22*(1), 47-61. https://doi.org/10.1080/00087114.1969.10796324
1261 Trolet, A., Baldrich, P., Criqui, M. C., Dubois, M., Clavel, M., Meyers, B. C., & Genschik, P. (2019).
1262 Cell Cycle-Dependent Regulation and Function of ARGONAUTE1 in Plants. *Plant Cell*,
1263 *31*(8), 1734-1750. https://doi.org/10.1105/tpc.19.00069
1264 Tsyganova, A. V., Brewin, N. J., & Tsyganov, V. E. (2021). Structure and Development of the
1265 Legume-Rhizobial Symbiotic Interface in Infection Threads. *Cells*, *10*(5).
1266 https://doi.org/10.3390/cells10051050
1267 Ursache, R., Andersen, T. G., Marhavy, P., & Geldner, N. (2018). A protocol for combining
1268 fluorescent proteins with histological stains for diverse cell wall components. *Plant J*, *93*(2),
1269 399-412. https://doi.org/10.1111/tpj.13784
1270 van Brussel, A. A., Bakhuizen, R., van Spronsen, P. C., Spaink, H. P., Tak, T., Lugtenberg, B. J., &
1271 Kijne, J. W. (1992). Induction of pre-infection thread structures in the leguminous host plant
1272 by mitogenic lipo-oligosaccharides of Rhizobium. *Science*, *257*(5066), 70-72.
1273 https://doi.org/10.1126/science.257.5066.70
1274 van Spronsen, P. C., Gronlund, M., Pacios Bras, C., Spaink, H. P., & Kijne, J. W. (2001). Cell
1275 biological changes of outer cortical root cells in early determinate nodulation. *Mol Plant*
1276 *Microbe Interact*, *14*(7), 839-847. https://doi.org/10.1094/MPMI.2001.14.7.839
1277 Vinardell, J. M., Fedorova, E., Cebolla, A., Kevei, Z., Horvath, G., Kelemen, Z., Tarayre, S., Roudier,
1278 F., Mergaert, P., Kondorosi, A., & Kondorosi, E. (2003). Endoreduplication mediated by the
1279 anaphase-promoting complex activator CCS52A is required for symbiotic cell differentiation
1280 in Medicago truncatula nodules. *Plant Cell*, *15*(9), 2093-2105.
1281 https://doi.org/10.1105/tpc.014373

1282 Weber, E., Engler, C., Gruetzner, R., Werner, S., & Marillonnet, S. (2011). A modular cloning system
1283 for standardized assembly of multigene constructs. *PloS One*, *6*(2), e16765.
1284 https://doi.org/10.1371/journal.pone.0016765
1285 Weimer, A. K., Biedermann, S., Harashima, H., Roodbarkelari, F., Takahashi, N., Foreman, J., Guan,
1286 Y., Pochon, G., Heese, M., Van Damme, D., Sugimoto, K., Koncz, C., Doerner, P., Umeda,
1287 M., & Schnittger, A. (2016). The plant-specific CDKB1-CYCB1 complex mediates
1288 homologous recombination repair in Arabidopsis. *EMBO J*, *35*(19), 2068-2086.
1289 https://doi.org/10.15252/embj.201593083
1290 Wildermuth, M. C., Steinwand, M. A., McRae, A. G., Jaenisch, J., & Chandran, D. (2017). Adapted
1291 Biotroph Manipulation of Plant Cell Ploidy. *Annu Rev Phytopathol*, *55*, 537-564.
1292 https://doi.org/10.1146/annurev-phyto-080516-035458
1293 Wipf, L., & Cooper, D. C. (1938). Chromosome Numbers in Nodules and Roots of Red Clover,
1294 Common Vetch and Garden Pea. *Proc Natl Acad Sci U S A*, *24*(2), 87-91.
1295 https://doi.org/10.1073/pnas.24.2.87
1296 Xiao, T. T., Schilderink, S., Moling, S., Deinum, E. E., Kondorosi, E., Franssen, H., Kulikova, O.,
1297 Niebel, A., & Bisseling, T. (2014). Fate map of Medicago truncatula root nodules.
1298 *Development*, *141*(18), 3517-3528. https://doi.org/10.1242/dev.110775
1299 Xiao, T. T., van Velzen, R., Kulikova, O., Franken, C., & Bisseling, T. (2019). Lateral root formation
1300 involving cell division in both pericycle, cortex and endodermis is a common and ancestral
1301 trait in seed plants. *Development*, *146*(20), dev182592. https://doi.org/10.1242/dev.182592
1302 Xu, J., Lee, Y. J., & Liu, B. (2020). Establishment of a mitotic model system by transient expression
1303 of the D-type cyclin in differentiated leaf cells of tobacco (Nicotiana benthamiana). *New*
1304 *Phytol*, *226*(4), 1213-1220. https://doi.org/10.1111/nph.16309
1305 Yang, W. C., de Blank, C., Meskiene, I., Hirt, H., Bakker, J., van Kammen, A., Franssen, H., &
1306 Bisseling, T. (1994). Rhizobium nod factors reactivate the cell cycle during infection and
1307 nodule primordium formation, but the cycle is only completed in primordium formation. *Plant*
1308 *Cell*, *6*(10), 1415-1426. https://doi.org/10.1105/tpc.6.10.1415
1309 Yant, L., & Bomblies, K. (2015). Genome management and mismanagement—Cell-level
1310 opportunities and challenges of whole-genome duplication. *Genes Dev*, *29*(23), 2405-2419.
1311 https://doi.org/10.1101/gad.271072.115
1312 Zanetti, M. E., Ripodas, C., & Niebel, A. (2017). Plant NF-Y transcription factors : Key players in
1313 plant-microbe interactions, root development and adaptation to stress. *Biochim Biophys Acta*
1314 *Gene Regul Mech*, *1860*(5), 645-654. https://doi.org/10.1016/j.bbagrm.2016.11.007
1315

FIGURES

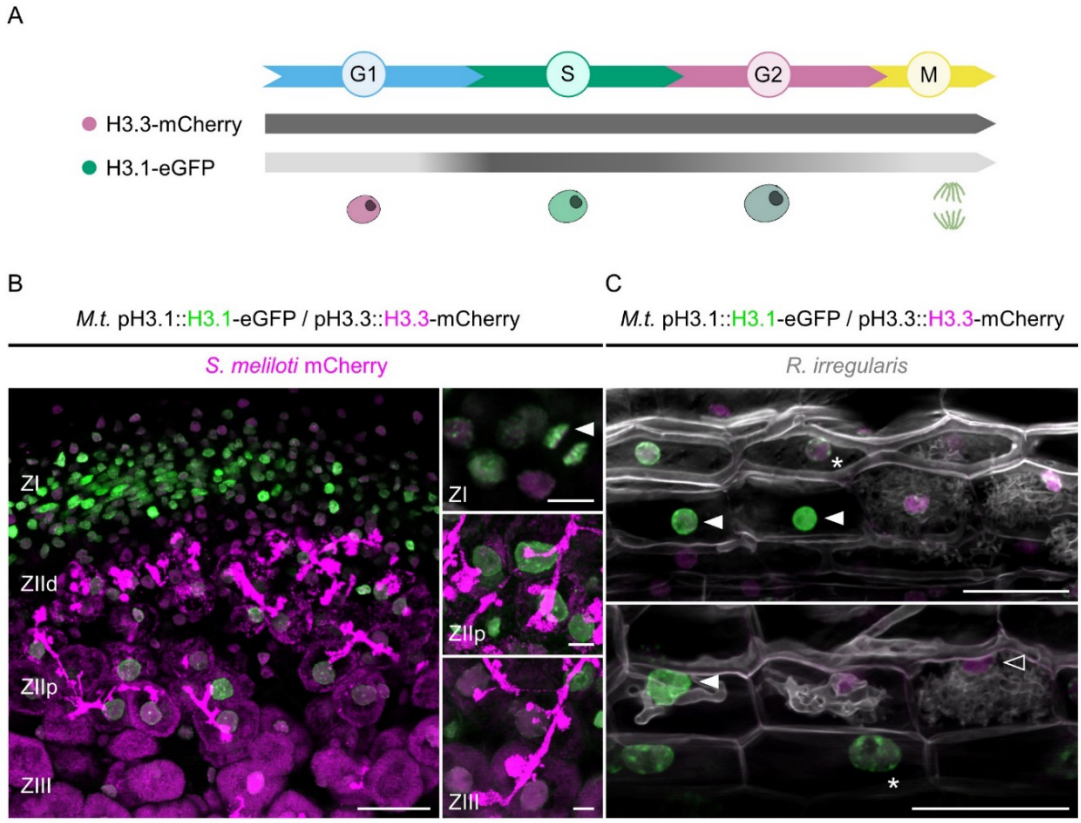

Figure 1. Medicago histone H3.1 patterns reveal sustained mitotic and endocycling activities in a symbiotic context. (**A**) Schematic representation of histone H3.3-mCherry and H3.1-eGFP distribution (horizontal bars) and fluorescence intensity (grey saturation) throughout the different cell-cycle phases (adapted from Echevarria et al., 2021). H3.1 is predominantly expressed during S-phase and incorporated during DNA replication in proliferating (G1, S, G2, M) and endocycling (G1, S, G2) cells. H3.3 is constitutively produced. Nuclei of increasing size and DNA content are coloured according to their H3.3 (pink) and H3.1 (green) content in decondensed chromatin (G1, S, G2) or condensed chromosomes (M). (**B**) Confocal images of nodule sections isolated from WT transgenic roots inoculated with mCherry-producing *S. meliloti* (35 to 40 dpi), showing H3.1-eGFP (green) and H3.3-mCherry (magenta) localization across characteristic developmental zones. H3.1 accumulates in the meristematic zone (ZI) enriched in proliferating cells (late-anaphase chromosomes indicated by a filled arrowhead) and in regions with high endoreduplication activity (ZIId and ZIIp, distal and proximal parts of the infection zone) where rhizobia are released into membrane-bound compartments called symbiosomes. H3.1 is extensively replaced by H3.3 in the fixation zone (ZIII) where host cells and rhizobia complete their differentiation process. Images are maximum intensity projections except the top-right panel (single focal plane). Scale bars: left panel = 50 µm; right panels = 10 µm. Transformation experiments were repeated 3 times with a total of 9 nodules from 6 composite plants showing similar results. (**C**) Confocal images of whole-mount WT roots colonized by *R. irregularis* (15 dpi). Plant and fungal cell walls were stained with Calcofluor white (grayscale). H3.1 was enriched in chromocenters (heterochromatin foci in nuclei indicated by stars) and kept at high levels in the euchromatin (diffuse labeling in nuclei pointed by filled arrowheads) from neighbouring (upper panel) and early-arbusculated cells (lower panel) of the inner cortical tissue. The empty arrowhead points to a nucleus with a low H3.1 content in a fully-arbusculated, differentiated cell. Images are maximum intensity projections. Scale bars: 50 µm. Two independent transformation experiments were performed with 3 to 5 composite plants analyzed per replica.

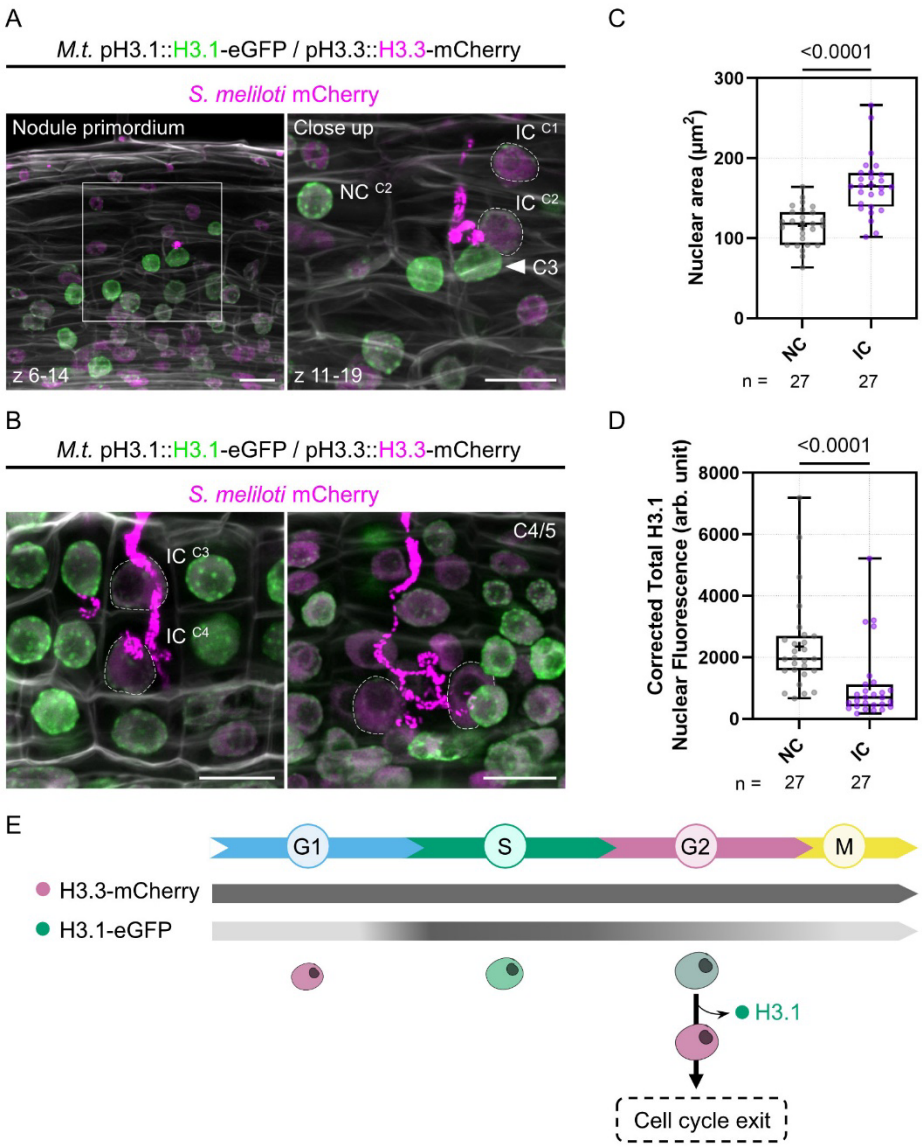

Figure 2. Individual reprogramming for infection includes large-scale chromatin rearrangements.
(**A-B**) Confocal images of whole-mount WT roots expressing the pH3.1::H3.1-eGFP / pH3.3::H3.3-mCherry reporter and inoculated with mCherry-producing *S. meliloti* (8 dpi). Images are maximum intensity projections (eGFP: green; mCherry: magenta; Calcofluor white cell-wall staining: grayscale). (**A**) Left panel: the solid-line frame indicates the outer and middle cortical regions of an early nodule primordium shown in the close up. Right panel: dotted-line regions of interest (ROIs) indicate nuclei of infected cells (IC) fully passed by a cortical infection thread in the first (C1) and second (C2) cortical layers. NC: neighbouring cell. The filled arrowhead points to the nucleus of a host cell from the middle cortical layer (C3), which is penetrated by the progressing infection thread. Scale bars: 20 µm. (**B**) Left panel: dotted-line ROIs indicate nuclei of infected cells (IC) being passed (C4) or recently passed (C3) by a cortical infection thread. Right panel: dotted-line ROIs indicate nuclei of infected cells in the inner cortex (C4/5) of a nodule primordium with several cell layers. Scale bars: 20 µm. (**C-D**) Quantification of the nuclear area (**C**) and corrected total H3.1-eGFP nuclear fluorescence (**D**) at the equatorial plane in couples of neighbouring (NC) and infected cells (IC) from the same cortical layer (C2 to C4, n = 27; see Materials and methods for more details). Roots from 2 to 7 composite plants with visible signs of inner cortical cell division (*i.e.*, showing high H3.1-eGFP signal) were analyzed from 3 independent transformation experiments. All data points are shown and crosses indicate sample means. Differences were statistically significant (P values < 0.0001) using an unpaired t-test with Welch's correction (**C**) or a Mann-Whitney test (**D**). (**E**) Schematic representation of histone H3.3-mCherry and H3.1-eGFP distribution (horizontal bars) and fluorescence intensity (grey saturation) throughout the different cell-cycle phases. Nuclei of increasing size and DNA content are coloured according to their merged H3.3 (magenta) and H3.1 (green) content in decondensed chromatin (G1, S, G2). This diagram illustrates cells exiting the cell cycle within proliferating or endoreduplicating populations, which proceed to a massive H3.1 eviction following their last DNA replication round (Otero et al., 2016).

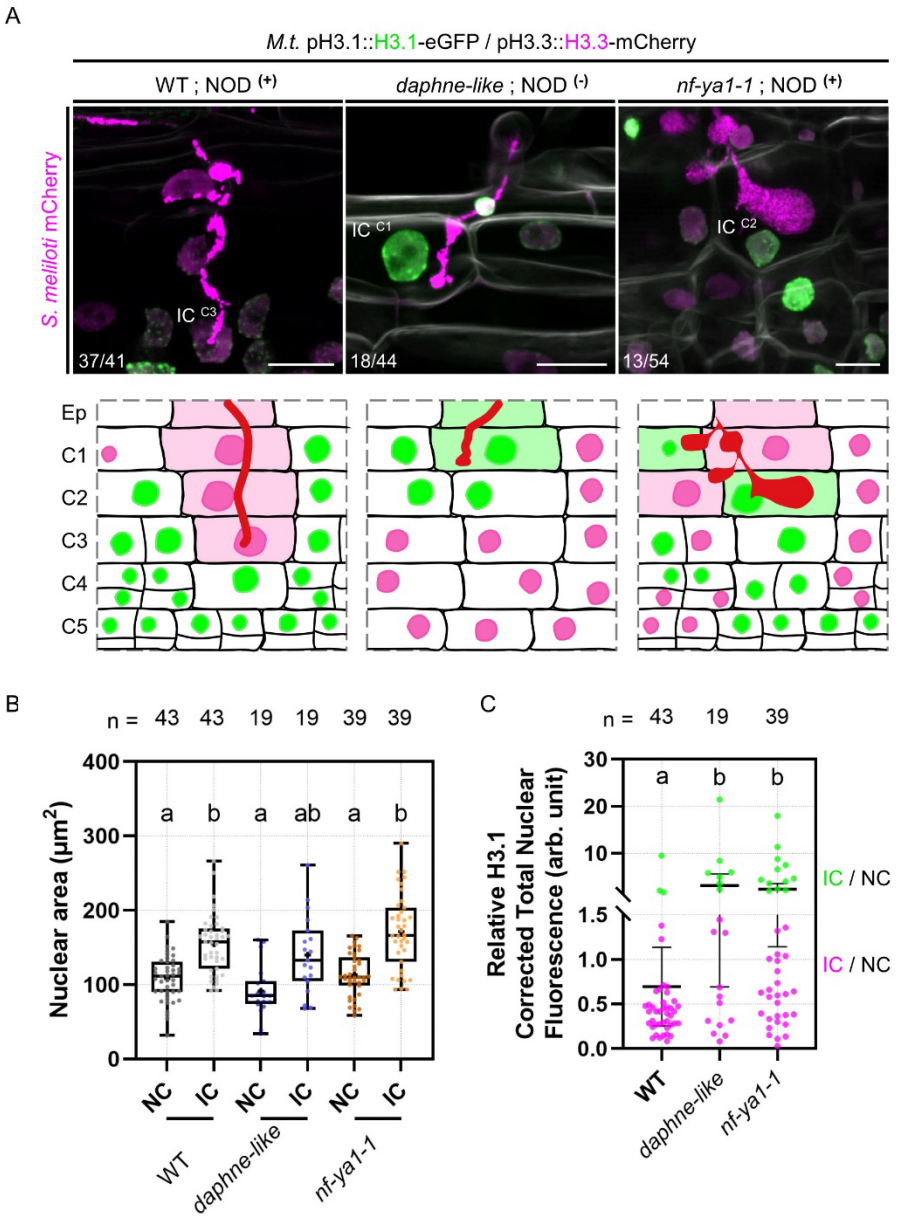

Figure 3. H3.1 eviction coincides with cortical infection thread progression.
(**A**) Confocal images of whole-mount transgenic roots co-expressing H3.1-eGFP and H3.3-mCherry in three different genotypes: WT (11 dpi), *daphne-like* (14 dpi) and *nf-ya1-1* (12 dpi), inoculated with mCherry-producing *S. meliloti*. WT and *nf-ya1-1* plants initiate nodule formation (NOD$^+$) whereas the *daphne-like* mutant is non-nodulating (NOD$^-$). Numbers indicate the frequencies of observation of a low (WT) or high (*daphne-like*, *nf-ya1-1*) H3.1-eGFP content in the last infected cortical cell. Corresponding schematic representations below each panel depict cellular proliferation or endocycling activities indicated by nuclear H3.1 levels (low: magenta; high: green) on the cortical infection thread trajectory (C1 to C3; diffuse magenta or green colouring) and in inner cortical layers (C4 to C5). Rhizobia inside infection threads are depicted in red. Confocal images are maximum intensity projections and show merged fluorescent channels (eGFP: green; mCherry: magenta; Calcofluor white cell-wall staining: grayscale in the middle and right panels). Scale bars: 20 µm. IC: infected cell. Ep: epidermis. (**B-C**) Quantification of the nuclear area (**B**) and the relative corrected total H3.1-eGFP nuclear fluorescence (IC/NC) (**C**) at the equatorial plane in couples of neighbouring (NC) and infected cells (IC) from the same cortical layer in WT (C1 to C4), *daphne-like* (C1 to C2) and *nf-ya1-1* (C1 to C4) genetic backgrounds (n = 43, 19 and 39 nuclei, respectively). Different letters indicate statistically significant differences according to a Kruskal-Wallis test followed by Dunn's multiple comparisons test. (**B**) All data points are shown and crosses indicate sample means. (**C**) All data points are shown with magenta or green indicating relative H3.1-eGFP nuclear signals (IC/NC) below 1,5 or above 1,6, respectively. Horizontal bars indicate sample means with 95% confidence interval. Ten to 21 composite plants (8-14 dpi) from 2 (*daphne-like*, *nf-ya1-1*) to 7 (WT) independent transformation experiments were analyzed.

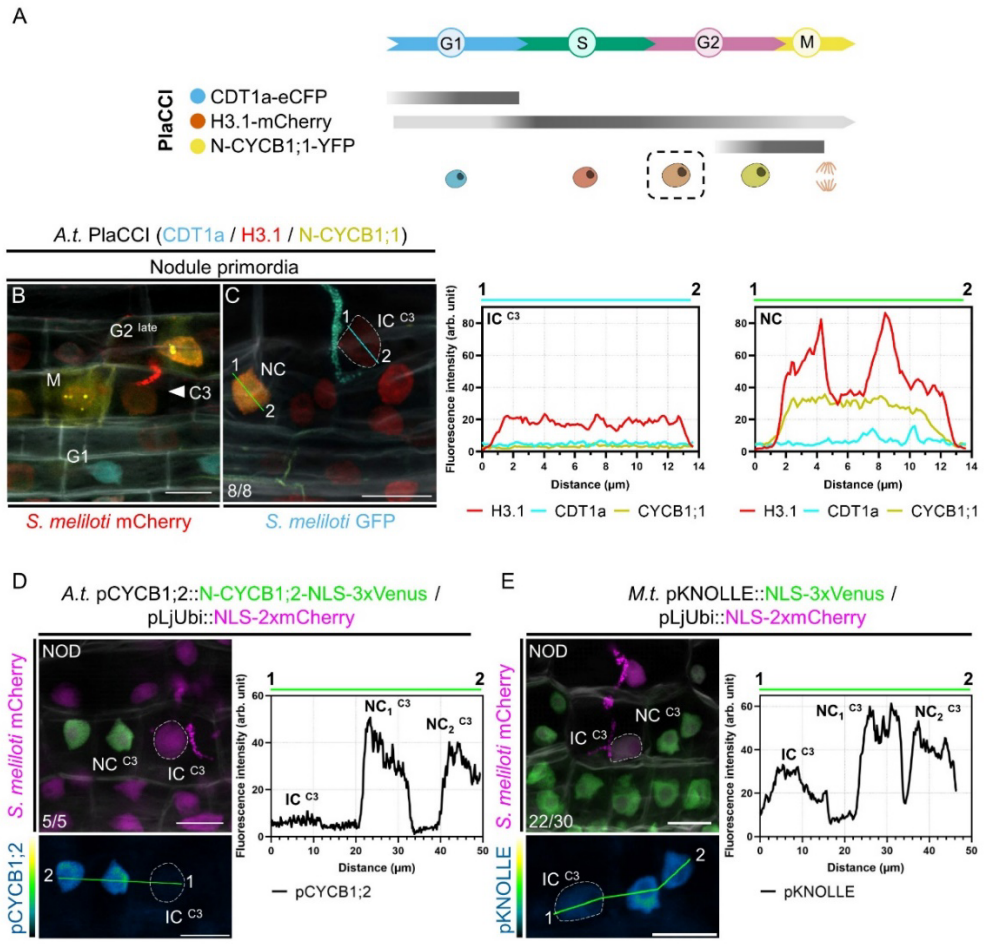

Figure 4. A tight control over host cells' mitotic commitment enables passage of the future nodule meristem. (**A**) Schematic representation of Arabidopsis CDT1a-eCFP, H3.1-mCherry and N-CYCB1;1-YFP distribution (horizontal bars) and fluorescence intensity (grey saturation) throughout the different cell-cycle phases (adapted from Echevarria et al., 2021; see also Desvoyes et al., 2020). CDT1a-CFP accumulates in G1 and is rapidly degraded during the G1/S transition (blunt end bar). H3.1 is predominantly expressed during S-phase and incorporated during DNA replication. N-CYCB1;1-YFP is present in late G2 and mitotic cells and is completely degraded in anaphase (blunt end bar). Nuclei of increasing size and DNA content are coloured according to their CDT1a (sky blue), H3.1 (vermillion) and N-CYCB1;1 (yellow) content in/around decondensed chromatin (G1, S, G2) or condensed chromosomes (M). H3.1 levels decrease in differentiating cells (dotted-line box). (**B-C**) Confocal images of whole-mount Medicago WT roots expressing the Arabidopsis PlaCCI reporter in nodule primordia at 7 dpi with mCherry- (**B**) or GFP-producing *S. meliloti* (**C**). Images are maximum intensity projections and show merged fluorescent channels (eCFP and GFP: cyan; mCherry: red; YFP: yellow; Calcofluor white cell-wall staining: grayscale). (**B**) The filled arrowhead points to a cell of the C3 layer penetrated by an infection thread. Cell-cycle phases of non-infected neighbouring cells are indicated. (**C**) Left panel: the dotted-line ROI indicates the nucleus of an infected cell (IC) from the C3 layer being passed by a cortical infection thread. Numbers indicate the frequencies of observation of the absence of CDT1a- or N-CYCB1;1-associated signals in the nucleus of the last infected cortical cell. Right panels: fluorescence intensity profiles of CDT1a-, H3.1- and N-CYCB1.1-associated signals along the cyan and green transects shown in (**C**). Scale bars: 20 µm. (**D**) Left panels: confocal images of a whole-mount WT root co-expressing a destabilized triple-Venus nuclear reporter driven by the Arabidopsis *CYCB1;2* promoter (pCYCB1;2::N-CYCB1;2-NLS-3xVenus) and a nuclear-localized tandem-mCherry as a transformation marker, 12 dpi with mCherry-producing *S. meliloti*. Numbers indicate the frequencies of observation of the absence of the triple-Venus reporter signal in the nucleus of the last infected cortical cell. Two independent transformation experiments were performed with 3 to 4 composite plants analyzed per replica. (**E**) Left panels: confocal images of a whole-mount WT root co-expressing a transcriptional reporter of Medicago *KNOLLE* driving a nuclear-localized triple-Venus (pKNOLLE::NLS-3xVenus) together with a nuclear-localized tandem-mCherry as a transformation marker, 12 dpi with mCherry-producing *S. meliloti*. Numbers indicate the frequencies of observation of nodule primordia where the triple-Venus reporter signal is kept comparably low on the cortical infection thread trajectory. A total of 12 composite plants from 2 independent transformation experiments were analyzed. (**D-E**) Images are maximum intensity projections and show merged fluorescent channels (Venus: green; mCherry: magenta; Calcofluor white cell-wall staining: grayscale in

1419 the upper panels). The Venus channel is shown in Green Fire Blue when isolated in lower panels, with blue or yellow
1420 indicating low or high fluorescence levels, respectively. The dotted-line ROIs indicate nuclei of infected cells (IC) from
1421 the C3 layer being passed by a cortical infection thread. The fluorescence intensity profiles of pCYCB1;2 and pKNOLLE
1422 reporter-associated signals along the green transects are shown in the corresponding right panels. NC: neighbouring cell.
1423 NOD: nodule primordium. Scale bars: 20 µm.
1424
1425

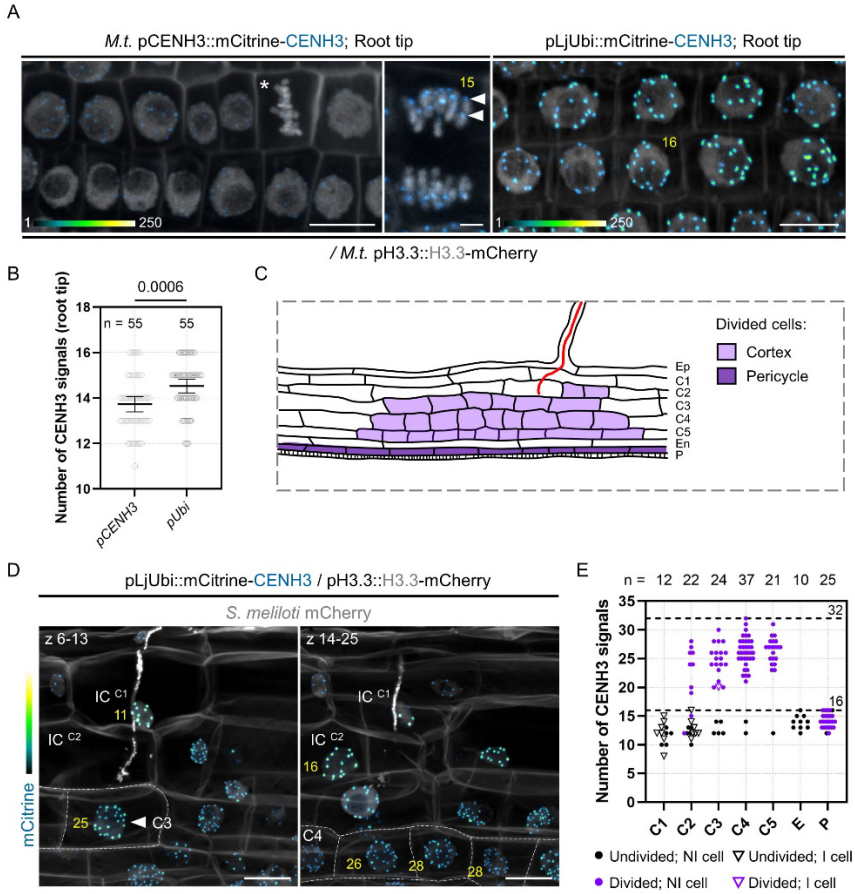

Figure 5. Dividing cortical cells initiating Medicago nodule primordium formation are tetraploid.
(**A**) Confocal images of whole-mount WT transgenic roots expressing mCitrine-CENH3 under the control of native (*M.t.* pCENH3; left and middle panels) or constitutive promoters (pLjUbi; right panel). Simultaneous expression of H3.3-mCherry enables the recognition of condensed (star) and segregating chromosomes (middle panel). mCitrine-CENH3 labels the centromeric region of individual chromosomes (filled arrowheads). The number of CENH3-labeled foci determined across image stacks is indicated in yellow. Images are maximum intensity projections and show merged fluorescent channels (mCitrine: Green Fire Blue; mCherry and Calcofluor white cell-wall staining: grayscale). In the Green Fire Blue colour scheme, blue or yellow indicate low or high fluorescence levels, respectively (min. to max. = 1-140 in the middle panel). Scale bars: left and right panels = 10 µm; middle panel = 2 µm. (**B**) Quantification of the number of centromeric signals in transgenic root tips expressing mCitrine-CENH3 under native (pCENH3) or constitutive (pUbi) promoters (n = 55 nuclei). All data points are shown and are from 2 (pUbi) to 3 (pCENH3) independent experiments with 7 composite plants analyzed per construct. Horizontal bars indicate sample means with 95% confidence interval. Differences were statistically significant (P value = 0.0006) using a Mann-Whitney test. (**C**) Schematic representation of an early nodule primordium where anticlinal cell divisions occurred in the pericycle (P; dark violet) and cortical cells (C2 to C5; light violet). Rhizobia inside the infection thread are depicted in red. Ep: epidermis. En: endodermis. (**D**) Maximum intensity projections of an early nodule primodium at the developmental stage represented in (**C**), formed in a WT root expressing the pLjUbi::mCitrine-CENH3 / pH3.3::H3.3-mCherry construct at 7 dpi with mCherry-producing *S. meliloti*. Dotted-line ROIs indicate the contours of divided cells in the inner (C4) and middle (C3) cortical layers. The number of CENH3-labeled foci, determined across image stacks and indicated in yellow are: 11 and 16 in undivided, infected cells (IC) from the outer cortical layers (C1; left panel and C2, right panel) and 25 to 28 in divided, uninfected cells from the C3 (filled arrowhead; left panel) and C4 layers (right panel). Images show merged fluorescent channels (mCitrine: Green Fire Blue; mCherry and Calcofluor white cell-wall staining: grayscale). In the Green Fire Blue colour scheme, blue or yellow indicate low or high fluorescence levels, respectively. Scale bars: 20 µm. (**E**) Quantification of the number of centromeric signals in early nodule primordia at the developmental stage depicted in (**C**), formed in inoculated WT roots (7 to 12 dpi) constitutively expressing mCitrine-CENH3. The number (n) of analyzed nuclei in each cell layer is indicated on the top. E: endodermis. P: pericycle. All data points are shown with black or violet symbols indicating undivided or divided cells, respectively. NI: non-infected cell (discs). I: infected cell (triangles). Horizontal dotted lines are positioned at y = 16 and y = 32, corresponding to diploid (2n = 16) or tetraploid (4n = 32) cellular states in Medicago. Data are from 2 independent experiments with 7 nodule primordia from 5 composite plants analyzed.

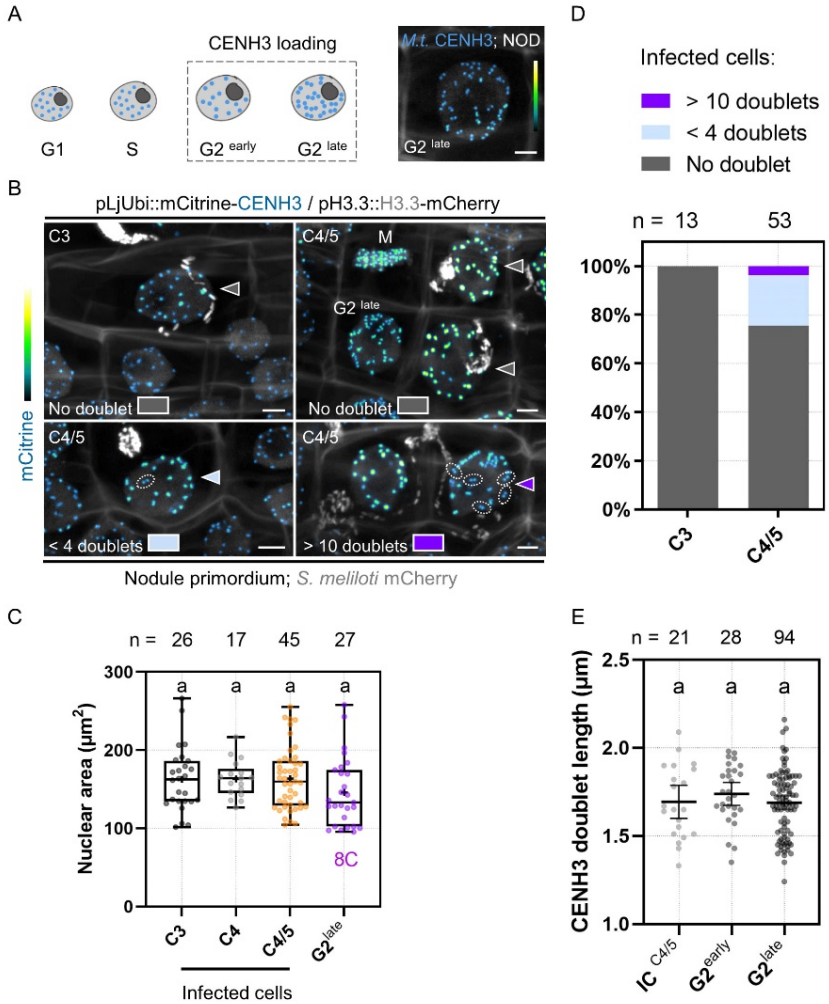

Figure 6. Primary infected nodule primordium cells do not reach full competence for chromosome segregation. (**A**) Schematic representation of CENH3 deposition at centromeres (blue dots) throughout the different pre-mitotic (G1, S, G2 ^{early} and G2 ^{late}) cell-cycle phases in plants. Nuclei of increasing size and DNA content are depicted as ovals. The dotted-line frame indicates the timing of CENH3 loading at replicated centromeres, occurring during G2 before sister kinetochore (blue doublets) split in preparation to mitosis (Lermontova et al., 2007). Right panel: confocal image of a late G2-phase cell observed in a nodule (NOD) in an inoculated WT transgenic root (12 dpi) constitutively expressing mCitrine-CENH3. The majority of fluorescent signals appear as doublets corresponding to sister kinetochores. Scale bar: 5 µm. (**B**) Confocal images of whole-mount WT roots expressing the pLjUbi::mCitrine-CENH3 / pH3.3::H3.3-mCherry construct and inoculated with mCherry-producing *S. meliloti* (7 to 12 dpi). Filled arrowheads point to nuclei of infected nodule primordium cells. Dotted-line ROIs indicate mCitrine-CENH3 doublets appearing as twin spots on the same focal plane. Neighbouring cells in late G2 or undergoing mitosis (M) are indicated. The presence of CENH3-labeled twin spots was assessed across image stacks in the nuclei of infected cells from the middle (C3) and inner (C4/5) cortical layers and colour-coded as follows: grey = no doublet (upper panels); light blue = 1 to 3 doublets (lower left panel); dark violet = 11 or more doublets (lower right panel). Scale bars: 5 µm. (**A-B**) Images are maximum intensity projections (mCitrine: Green Fire Blue; mCherry and Calcofluor white cell-wall staining: grayscale). In the Green Fire Blue colour scheme, blue or yellow indicate low or high fluorescence levels, respectively. (**C**) Quantification of the nuclear area at the equatorial plane in cells being passed by a cortical infection thread (infected cells) in nodule primordia formed by WT transgenic roots inoculated with *S. meliloti* (7 to 12 dpi). The number (n) of analyzed nuclei in each cell layer (C3 to C4/5) is indicated on the top. The 8C chromatin-value is given for uninfected nodule primordium cells in late G2 showing close to 32 mCitrine-CENH3 doublets as identified in (**A**) and (**B**). All data points are shown and crosses indicate sample means. Differences were not statistically significant according to a Kruskal-Wallis test followed by Dunn's multiple comparisons test. At least 9 composite plants from 2 independent experiments were analyzed. (**D**) Quantification of infected cells in C3 (n = 13) and C4/5 (n = 53) cortical layers in nodule primordia, showing no doublet (grey), 1 to 3 doublets (light blue) or more than 11 doublets (dark violet) labelled by mCitrine-CENH3. Nine composite plants from 2 independent experiments were analyzed. (**E**) Quantification of the length of mCitrine-CENH3 doublets appearing as twin spots on the same focal plane in infected cells (IC) from the C4/5 cortical layer (n = 11), early G2 (n = 12) and late G2-

1487 phase cells (n = 27) in nodule primordia. n = 21 (IC $^{C4/5}$), 28 (G2^{early}), 94 (G2^{late}) doublets. Horizontal bars indicate sample
1488 means with 95% confidence interval. Differences were not statistically significant according to a Kruskal-Wallis test
1489 followed by Dunn's multiple comparisons test. All data points are shown and are from 6 to 10 composite plants from 2
1490 independent transformation experiments.
1491

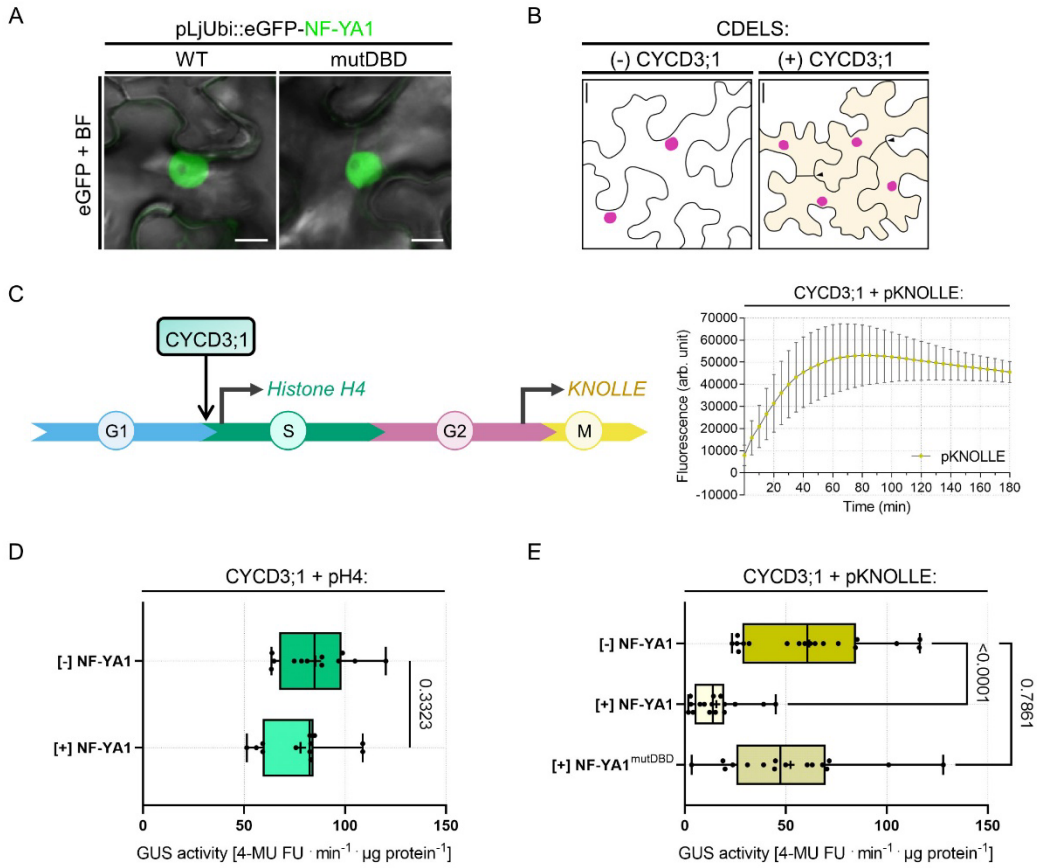

Figure 7. NF-YA1 specifically reduces the expression of a G2/M gene in a cell-division enabled system. (**A**) Live-cell confocal images of *N. benthamiana* epidermal cells ectopically expressing eGFP-NF-YA1 variants: WT (left panel) or impaired in DNA recognition (mutDBD; right panel). Both fusion proteins accumulate in the nucleus and were used in fluorometric β-glucuronidase (GUS) assays. Images are maximum intensity projections and show merged fluorescent (eGFP: green) and bright field (BF) channels. Scale bars: 10 µm. (**B**) Schematic representation of the cell division-enabled leaf system (CDELS) on the scale of epidermal pavement cells in *N. benthamiana*. Differentiated cells in mature leaves (left panel) re-enter the canonical cell cycle upon ectopic expression of the Arabidopsis D-type cyclin CYCD3;1 (right panel). Nearly all re-activated pavement cells (diffuse yellow colouring) have completed cytokinesis after 3 days (filled arrowheads). See also Figure 7 – figure supplement 2B. Scale bars: 20 µm. (**C**) Left panel: schematic representation of the CDEL system on the scale of the canonical cell cycle. Ectopically-expressed CYCD3;1 targets and activates cyclin-dependent kinases (CDK, not shown), fostering the G1/S transition. Progression throughout the different cell-cycle phases is accompanied by the sequential activation of DNA synthesis (S) and mitotic genes (M). Histone *H4* and *KNOLLE* promoter-reporters were selected as readouts for G1/S and late G2/M transcriptional waves, respectively. Right panel: fluorometric GUS assay in tobacco leaf cells ectopically expressing CYCD3;1 and the Medicago pKNOLLE::GUS (pKNOLLE) reporter construct. Fluorescence curves (GUS-mediated hydrolysis of 4-MUG) over time are shown for 3 biological replicates. Error bars indicate standard deviation. Data are from 1 of 4 independent transient transformations. (**D**) Activity of GUS driven by the histone *H4* promoter (pH4) in the absence or presence of ectopically-expressed eGFP-NF-YA1 (NF-YA1) in CDEL samples (+ CYCD3;1). All data points are shown and crosses indicate sample means. Differences were not statistically significant (P value = 0.3323) according to an unpaired t test with Welch's correction. Data are from 3 independent transformation experiments. n = 12 ([-] NF-YA1) and 12 ([+] NF-YA1) biological samples. (**E**) Activity of GUS driven by the *KNOLLE* promoter (pKNOLLE) in CDEL samples (+ CYCD3;1) in the absence or presence of ectopically-expressed eGFP-NF-YA1 variants with WT (NF-YA1) or mutated DNA-binding domain (NF-YA1^{mutDBD}). All data points are shown and crosses indicate sample means. Statistically significant differences ([-] NF-YA1 versus [+] NF-YA1; P value < 0.0001) or non-significant differences ([-] NF-YA1 versus [+] NF-YA1^{mutDBD}; P value = 0.7861) are based on a Kruskal-Wallis test followed by Dunn's multiple comparisons test. Data are from 4 to 5 independent transformation experiments. n = 18 ([-] NF-YA1), 16 ([+] NF-YA1), 16 ([+] NF-YA1^{mutDBD}) biological samples.

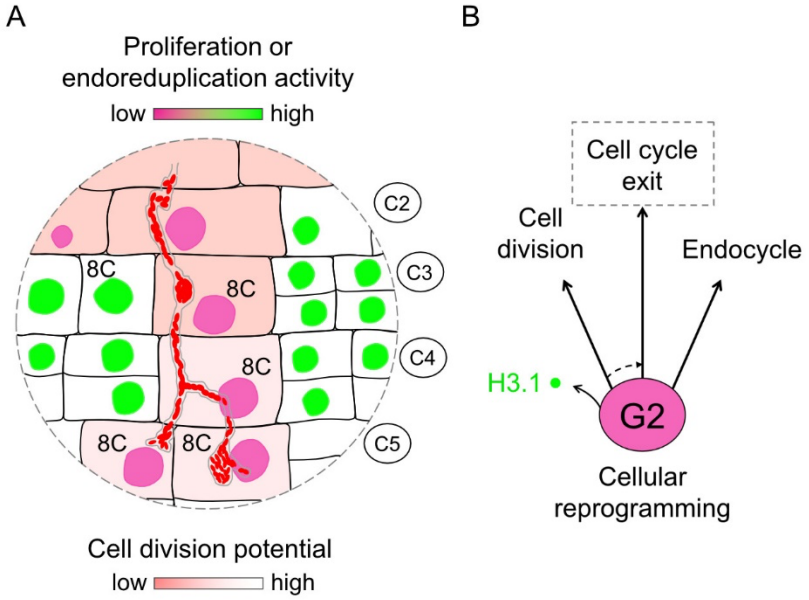

Figure 8. Model illustrating characteristic cellular traits on the cortical infection thread trajectory.
(**A**) Cortical cells competent for sustained transcellular infection thread progression are characterized by a reduced proliferation or endoreduplication activity (pink to green two-colour gradient). By the time they are crossed and ultimately internalize bacteria, such tetraploid cells (this study, Torrey and Barrios, 1969) reach a post-replicative, 8C ploidy stage but contrary to direct neighbour cells, they do not commit to a subsequent cell division (red to white two-colour gradient). (**B**) Rather, cells supporting transcellular infection presumably enter a prolonged G2-phase (this study, Yang et al., 1994) during which they remodel their histone H3 composition as part of their cellular reprogramming for infection. This differentiation process and concurrent transcellular passage are accomplished within a last cell-cycle round. We propose that cellular factors controlling the G2/M transition and eventually the exit from the canonical cell cycle (dashed arrow) are prominent candidates to support intracellular infection competence.